Mon. Not. R. Astron. Soc. **000**, 1–26 (2014) Printed 31 October 2014 (MN LATEX style file v2.2)

The Nature and Origin of Substructure in the Outskirts of M31 – II. Detailed Star Formation Histories⋆

Edouard J. Bernard,[1]† Annette M. N. Ferguson,[1] Jenny C. Richardson,[1,2] Mike J. Irwin,[2] Michael K. Barker,[1] Sebastian L. Hidalgo,[3,4] Antonio Aparicio,[3,4] Scott C. Chapman,[2,5] Rodrigo A. Ibata,[6] Geraint F. Lewis,[7] Alan W. McConnachie,[8] Nial R. Tanvir[9]

[1]*SUPA, Institute for Astronomy, University of Edinburgh, Royal Observatory, Blackford Hill, Edinburgh EH9 3HJ, UK*
[2]*Institute of Astronomy, Madingley Road, Cambridge, CB3 0HA, UK*
[3]*Instituto de Astrofísica de Canarias, Calle Vía Láctea s/n, 38205 La Laguna, Tenerife, Spain*
[4]*Departamento de Astrofísica, Universidad de La Laguna, 38200 Tenerife, Spain*
[5]*Department of Physics and Atmospheric Science, Dalhousie University, 6310 Coburg Road, Halifax, Nova Scotia B3H 4R2, Canada*
[6]*Observatoire Astronomique de Strasbourg, Université de Strasbourg, CNRS, UMR 7550, 11 rue de l'Université, F-67000 Strasbourg, France*
[7]*Institute of Astronomy, School of Physics, University of Sydney, NSW 2006, Australia*
[8]*NRC Herzberg Institute for Astrophysics, 5071 West Saanich Road, Victoria, V9E 2E7, British Columbia, Canada*
[9]*Department of Physics & Astronomy, University of Leicester, Leicester LE1 7RH, UK*

arXiv:1406.2247v2 [astro-ph.GA] 30 Oct 2014

Accepted –. Received –; in original form –

ABSTRACT

While wide-field surveys of M31 have revealed much substructure at large radii, understanding the nature and origin of this material is not straightforward from morphology alone. Using deep HST/ACS data, we have derived further constraints in the form of quantitative star formation histories (SFHs) for 14 inner halo fields which sample diverse substructures. In agreement with our previous analysis of colour-magnitude diagram morphologies, we find the resultant behaviours can be broadly separated into two categories. The SFHs of 'disc-like' fields indicate that most of their mass has formed since $z \sim 1$, with one quarter of the mass formed in the last 5 Gyr. We find 'stream-like' fields to be on average 1.5 Gyr older, with $\lesssim$10 percent of their stellar mass formed within the last 5 Gyr. These fields are also characterised by an age–metallicity relation showing rapid chemical enrichment to solar metallicity by $z = 1$, suggestive of an early-type progenitor. We confirm a significant burst of star formation 2 Gyr ago, discovered in our previous work, in all the fields studied here. The presence of these young stars in our most remote fields suggests that they have not formed *in situ* but have been kicked-out from the thin disc through disc heating in the recent past.

Key words: galaxies: individual: M31 – Local Group – galaxies: formation – galaxies: evolution – galaxies: haloes – galaxies: stellar content

1 INTRODUCTION

Galaxy evolution proceeds dynamically through interactions, accretions and mergers with other dark matter halos and through the formation and evolution of the stars within them. Such events may influence the local star formation rate and/or add new material directly from the tidal disruption of satellite galaxies. The fossil record of a galaxy's history is encoded within the detailed properties of its stellar populations. Over the last decade, a variety of methods have been applied to mine this information in both the local and distant Universe.

Retrieving the star formation history (SFH) from a deep colour-magnitude diagram (CMD) is one of the most powerful tools available for understanding galaxy assembly. Since stars occupy very specific loci on the CMD depending on their evolutionary phases, the morphology of a CMD can be interpreted in terms of the underlying composition of the parent population. By comparing an observed CMD with a large library of synthetic CMDs constructed from theoretical stellar evolution models and various input parameters (e.g. initial mass function [IMF], binary fractions), the

⋆ Based on observations made with the NASA/ESA Hubble Space Telescope, obtained at the Space Telescope Science Institute, which is operated by the Association of Universities for Research in Astronomy, Inc., under NASA contract NAS5-26555. These observations are associated with programmes GO-9458 and GO-10128.

† E-mail: ejb@roe.ac.uk

© 2014 RAS

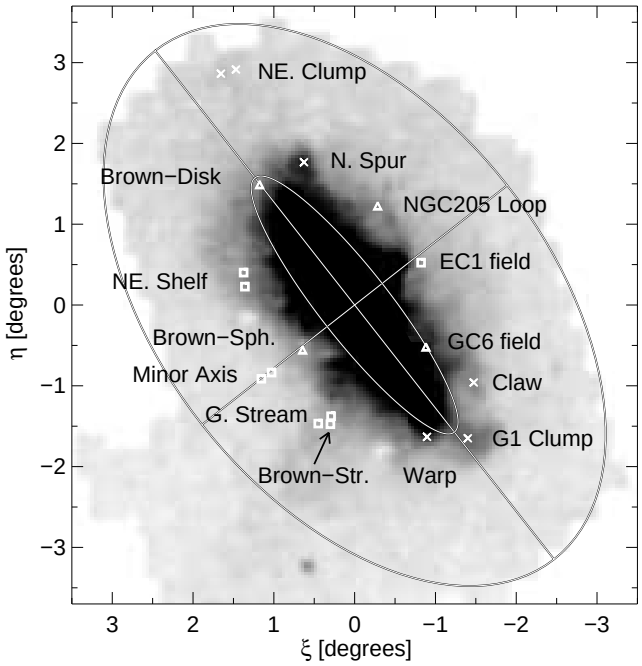

Figure 1. Locations of our *HST/ACS* pointings superimposed onto the INT/WFC map of M31's inner halo (Irwin et al. 2005), showing the distribution of evolved giant stars around M31. Crosses, open squares, and open triangles represent the disc-like, stream-like, and composite fields (see text for details). The image spans 95 kpc × 100 kpc and each ACS field covers $0.8 \text{ kpc} \times 0.8 \text{ kpc}$ at the distance of M31. All of the significant substructure discovered during the course of the INT/WFC survey is sampled by our data. The inner ellipse has a semimajor axis of 2° (27 kpc) and represents an inclined disc with $i = 77.^{\circ}5$ and position angle of $38.^{\circ}1$. The outer ellipse, of semimajor axis length 4° (55 kpc), roughly indicates the spatial extent of the INT survey.

temporal evolution of the star formation rate and chemical enrichment history can be extracted.

Quantitative star formation history work is, to some extent, still in its infancy. While a great deal of progress has been made in charting the SFHs of dwarf galaxies in the Local Group (LG; see Tolstoy, Hill, & Tosi 2009; Weisz et al. 2014, and references therein), these constitute only a small fraction of the local stellar mass density. In the Milky Way, our knowledge of the detailed SFH is essentially confined to a $\lesssim$ 100 pc region in the disc around the Sun, and even then with large uncertainties at both young ($\lesssim$ 1 Gyr) and old ($\gtrsim$ 7 Gyr) ages (e.g. Cignoni et al. 2006). The SFH across the M33 disc is reasonably well known (Williams et al. 2009; Barker et al. 2011) but a much less detailed picture exists for our sister galaxy, M31. This is due in part to the large angular size of M31 on the sky and the fact that the inner ∼20 kpc has a high stellar density and significant differential reddening (e.g. Bedin 2010; Dalcanton et al. 2012), hindering the ability to reliably probe the ancient SFH of the main body.

Resolving the oldest main-sequence turn-off (MSTO) stars in M31 – crucial for completely breaking the age–metallicity degeneracy – requires many orbits of the *HST* (e.g. Brown et al. 2003); yet a single Advanced Camera for Surveys *ACS* field (0.8×0.8 kpc at the distance of M31) captures but a tiny fraction of the galaxy's extent. One of the first attempts to extract the detailed SFH in M31 back to early epochs was carried out by Brown et al. (2006). These authors obtained ultra-deep *HST/ACS* imaging of three fields (nominally in the outer disc, giant stellar stream [GSS] and halo) down to the oldest MSTO. They found evidence for extended star formation and strong intermediate-age components (ages $\sim 4 - 8$ Gyr), with slight variations from field to field. Unfortunately, interpreting these results in the context of the M31's formation history was not straightforward given the rich substructure present in all the fields. More recently, we have explored the SFH of a field located in the south-western warp of the main disc (Bernard et al. 2012). Our derived SFH is far from smooth and includes the presence of a strong burst of star formation about 2 Gyr ago that lasted about 1 Gyr and contributed ∼25 percent of the total mass of stars formed in this field. Given the M33 outer disc exhibits a concurrent burst of star formation (Barker et al. 2011; Bernard et al. 2012), we suggested that these bursts might have been triggered by an interaction between the two galaxies. Indeed, self-consistent N-body modeling of the M31-M33 system suggests that their last perigalactic passage occurred at about this epoch (McConnachie et al. 2009).

The highly structured nature of M31's outer regions has been revealed by a number of wide-field imaging surveys over the last decade (e.g. Ibata et al. 2001; Ferguson et al. 2002; Ibata et al. 2007; Tanaka et al. 2010; Ibata et al. 2014). Various features are observed, such as streams, loops and shells, however it is difficult to constrain the origin of this material on the basis of its morphology alone. While such features are often associated with accretions of small dwarf galaxies, it is also possible that much of the material is simply disrupted and heated disc that has been kicked out during a recent encounter (e.g. Kazantzidis et al. 2008). In attempt to decipher the nature and origin of the brightest substructures in M31, we have undertaken a deep *HST/ACS* survey of 14 fields in the inner halo and outer disc, many of which lie on discrete stellar substructures. Our fields span projected galactocentric radii of 12 kpc $\lesssim \text{R}_{proj} \lesssim$ 45 kpc and are deep enough to resolve individual stars down to three magnitudes below the horizontal-branch (HB). Richardson et al. (2008) presented a comparative analysis of the CMDs of these fields which led to the conclusion that the substructure seen had two distinct origins. Five of the fields have stellar populations identical to those of the GSS, the progenitor of which is a putative $\sim 10^9 - 10^{10}$ $\text{M}_{\odot}$ galaxy that was cannibalised by M31 some time in the recent past (Fardal et al. 2007). Another five fields show evidence for moderately young populations, consistent with them having once been part of the thin disc of M31 and subsequently heated by a tidal ancounter. The remaining four fields show evidence of both stream-like and disc-like stellar populations mixed together, which Richardson et al. (2008) termed as composite fields.

Here we extend the analysis of Richardson et al. (2008) by using the technique of synthetic CMD fitting to provide a more detailed and robust quantitative analysis of these fields. The method is fully consistent with that presented in Bernard et al. (2012); the drawback is that our photometry is slightly shallower (∼1 mag) and therefore does not capture the oldest MSTOs with good signal-to-noise. This limits the information available about the earliest epochs of star formation and tends to blur the age–metallicity relation (AMR). The paper is structured as follows: in Section 2, we present the observations and the data reduction steps. The CMD-fitting method is described in Section 3, along with the resulting SFHs. Our interpretation of the results is discussed in Section 4, and a summary of the main results is given in Section 5.

Table 1. Field Information.

Field name	Type[a]	R.A. (J2000)	Dec. (J2000)	E(B − V)[b]	R_{proj}[c] (kpc)	R_{disc}[d] (kpc)
G Stream[e]	S	00:44:15.5	39:53:30.0	0.058	19.0	79.5
		00:45:05.0	39:48:00.0	0.051	20.7	68.4
Brown-stream	S	00:44:18.0	39:47:36.0	0.053	20.3	72.7
Minor Axis[e]	S	00:48:08.4	40:25:30.0	0.060	17.9	91.8
		00:48:47.8	40:20:44.6	0.059	19.9	82.7
EC1_field	S	00:38:19.5	41:47:15.4	0.070	13.2	60.5
NE Shelf[e]	S	00:49:59.4	41:28:55.5	0.065	18.6	54.3
		00:50:05.7	41:39:21.4	0.071	19.3	59.5
G1 Clump	D	00:35:28.0	39:36:19.1	0.063	29.2	29.7
Warp	D	00:38:05.1	39:37:54.9	0.054	25.1	31.1
Claw	D	00:35:00.3	40:17:37.3	0.060	23.7	42.0
N Spur	D	00:46:10.0	43:02:00.0	0.079	25.3	43.3
NE Clump[e]	D	00:51:56.7	44:06:38.5	0.093	44.1	59.0
		00:50:55.2	44:10:00.4	0.092	44.6	53.0
GC6_field	C	00:38:04.6	40:44:39.8	0.074	13.8	26.1
NGC205 Loop	C	00:41:11.6	42:29:43.1	0.076	17.0	71.5
Brown-disk	C	00:49:08.5	42:44:57.0	0.080	25.6	25.6
Brown-spheroid	C	00:46:08.1	40:42:36.4	0.081	11.5	53.0

[a] S: stream-like; D: disc-like; C: composite.
[b] Values from Schlegel, Finkbeiner & Davis (1998).
[c] Projected radial distance.
[d] Radii within the disc plane calculated assuming an inclined disc with $i = 77.5^\circ$ and a position angle of 38.1°.
[e] Low stellar density fields that required two adjacent pointings.

2 OBSERVATIONS AND DATA REDUCTION

2.1 The Dataset

The dataset consists of 14 deep HST/ACS fields in the inner halo and outer disc of M31 and it has been fully described in Richardson et al. (2008). Nine of the fields were chosen to specifically sample stellar substructures in the inner halo of M31 (proposals GO-9458 and GO-10128; P.I.: A. Ferguson). Another two fields were observed as part of our imaging survey of halo globular clusters (GO-10394; P.I.: N. Tanvir); to study the background M31 field populations, we have masked the clusters by removing all the stars within their respective tidal radii (Barmby et al. 2007; Tanvir et al. 2012). The last three fields are archival data from ultra-deep imaging programs (GO-9453 and GO-10265; P.I.: T. Brown) targeting the outer disc, spheroid, and the GSS.

Figure 1 shows the location of our fields superimposed onto the INT/WFC map of the outer disc and inner halo of M31. Most targets were observed via a single pointing but the low stellar density in four fields required two adjacent pointings to be obtained. While the data analysed in this work typically comprises three *HST* orbits per pointing, some of the fields were originally observed for considerably longer. As explained in Richardson et al. (2008), we have analysed only a subset of these data in order to match the depth of our other *HST/ACS* fields and allow a homogeneous comparison. Table 1 contains information about the location of the fields, their distance from the centre of M31, and their colour excess from Schlegel, Finkbeiner & Davis (1998). We also indicate whether the fields were identified as disc-like (D), stream-like (S) or composite (C) on the basis of CMD morphology by Richardson et al. (2008). The substructures probed by our fields are briefly described below.

• The *NE Clump*[1] probes a large (1° ≈ 13 kpc in diameter) diffuse over-density of stars over 40 kpc away from the centre of M31 along the north-eastern major axis. This clump of stars appears to be connected to M31 by a faint filament. Using shallow SDSS imaging reaching the tip of the red giant branch (RGB), Zucker et al. (2004) noted a similarity between the stellar populations of the NE Clump and the G1 Clump (see below). They suggest the two may have been torn off from the thin disc or part of an ancient tidal stream, or that the NE Clump is a satellite galaxy of M31 undergoing tidal disruption. Kniazev et al. (2014) recently suggested a possible association with the GSS on the basis of planetary nebula kinematics.

• The *NGC205 Loop* field probes an arc of material in the inner halo of M31 which appears to emanate from the dwarf elliptical satellite, NGC 205. The RGB colour and kinematics suggest that this loop could be material tidally stripped from NGC 205 (McConnachie et al. 2004; McConnachie 2005; Ibata et al. 2005).

• The *Claw*, named for its peculiar morphology, is a significant substructure which protrudes from south-western part of the disc.

• The *G1 Clump* samples the prominent over-density of stars (∼12 kpc in diameter) on the south-western major axis. Originally named for its proximity to the nearby massive globular cluster G1, subsequent stellar population analyses have since discounted a link between the two (Rich et al. 2004; Faria et al. 2007). Meanwhile, Keck spectroscopy has shown that the kinematics of the G1 Clump stars have more in common with the neutral hydrogen disc of M31 than with either the G1 globular cluster or the stellar halo (Reitzel, Guhathakurta & Rich 2004; Ibata et al. 2005).

[1] From here on we use italicised font for the name of our fields, to distinguish them from the name of the substructure they probe.

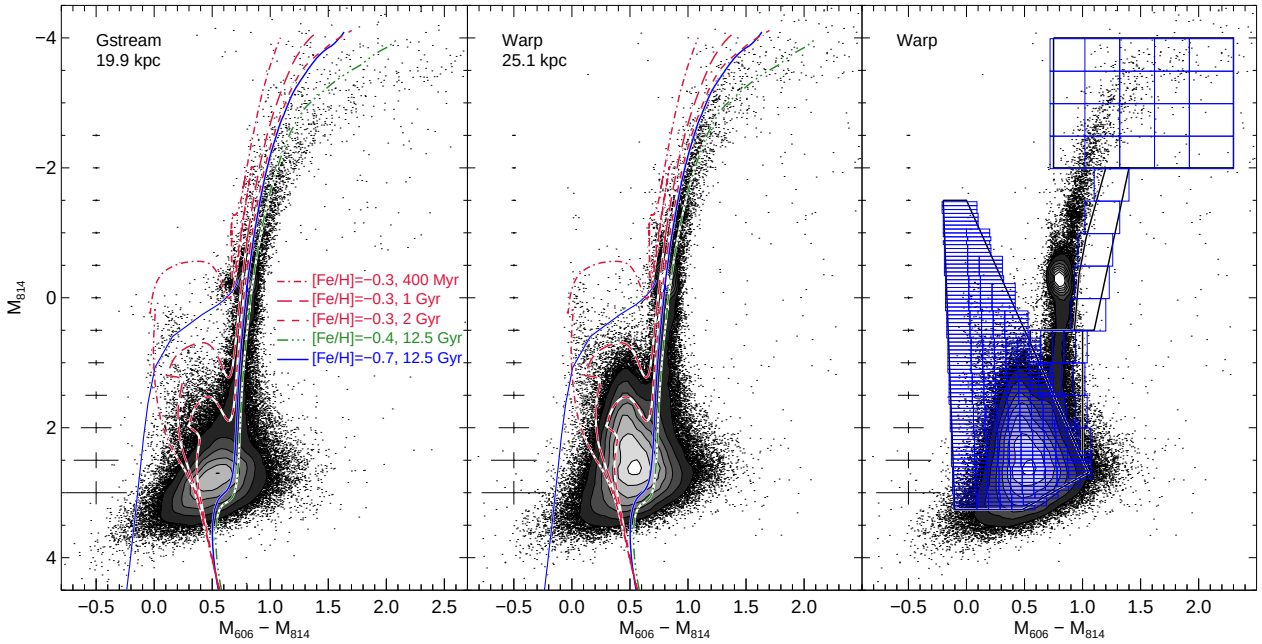

Figure 2. Colour-magnitude diagrams for the *Giant Stream* (left) and the *Warp* (middle) fields, where selected isochrones and a ZAHB from the BaSTI library (Pietrinferni et al. 2004) are overlaid. The error bars show the mean photometric errors as a function of magnitude. The projected radial distances are indicated in each panel. The contour levels correspond to $[15, 25, 35, 45, 55, 65, 75]\times10^3$ stars mag^{-2}. The black and blue lines in the right panel show the location of the regions ('bundles') and the boxes, respectively, used for the CMD-fitting (see Section 3.1), overplotted on the *Warp* CMD.

• The stellar and gaseous discs of M31 are warped at large radii (e.g., Innanen et al. 1982; Brinks & Burton 1984; Walterbos & Kennicutt 1988); the *Warp* and *NSpur* probe the periphery of the warped disc on opposite sides of the galaxy.

• The *NE Shelf* samples a major shelf-like over-density in the north-east side of the disc. Ferguson et al. (2005) have shown that the CMD morphology of the NE Shelf and a region of the GSS bear striking resemblance. Indeed, N-body simulations by Fardal et al. (2007) suggest that both the Western Shelf (see below) and the NE Shelf might be debris from a forward wrap of the GSS progenitor.

• The *EC1_field* samples a section of the diffuse Western Shelf feature of the Northern minor axis, near the old extended cluster EC1 (Tanvir et al. 2012). This vast structure was first studied in detail by Fardal et al. (2012).

• The *GC6_field* and *Brown-disk* sample portions of the outer disc of M31.

• The *Giant Stream* and *Brown-stream* fields probe the eponymous GSS of tidal debris falling into the far side of M31. Over 100 kpc in length (Ibata et al. 2007) this accretion event dominates the inner halo of M31 and may be related to the North-Eastern and Western Shelves.

• The two fields lying along the Southern minor axis, the *Minor Axis* and *Brown-spheroid*, were chosen to probe the underlying halo of M31. They were selected because it was initially believed that they were free from substructure. However, subsequent wide-field mapping as well as the analysis of Richardson et al. (2008) showed that both fields are significantly contaminated by GSS material.

2.2 Photometry and artificial star tests

For homogeneity with the analysis presented in Bernard et al. (2012), we redid the photometry and artificial star tests following identical methods.[2] The only difference here is the point spread functions (PSFs) that were used. Due to a bug in the CALACS processing pipeline, the pixels affected by cosmic rays were not flagged in the data quality arrays, which complicated the creation of the model PSF for each ACS chip image. Instead, we created PSFs by stacking the 8 (12) images in F606W (F814W) of the *Warp* field data of Bernard et al. (2012) and selecting over 200 isolated stars per stacked image. The residuals in the PSF-subtracted images obtained with these PSFs are significantly smaller than when using PSFs created from the images affected by cosmic rays.

The stellar photometry was carried out on the individual exposures with the standard DAOPHOT/ALLSTAR/ALLFRAME suite of programs (Stetson 1994). The catalogues were then corrected for foreground reddening using the extinction maps of Schlegel, Finkbeiner & Davis (1998); no further correction was necessary since the resulting CMDs showed no evidence of differential reddening. They were also cleaned of non-stellar objects by applying cuts on the photometric parameters given by ALLFRAME, namely the photometric uncertainty ($\sigma \leqslant 0.3$) and the sharpness, describing how much broader the profile of the object appears compared to the profile of the PSF ($|\mathtt{SHARP}| \leqslant 0.3$). Finally, we converted the observed CMDs to absolute magnitudes – as needed to calculate the SFH – using the approximate distance obtained from the mean magnitude of the red clump (RC) stars. We emphasize the fact that the SFH calculations do not require a precise distance, as the algorithm minimizes the impact of the distance uncertainties by shifting the observed CMD with respect to the synthetic CMD to find the best solution.

Sample CMDs are shown in the left and middle panels of Figure 2, where isochrones and a zero-age horizontal-branch (ZAHB)

[2] the photometric catalogue, artificial star tests, and output of the SFH calculations for each field are available on request to the authors.

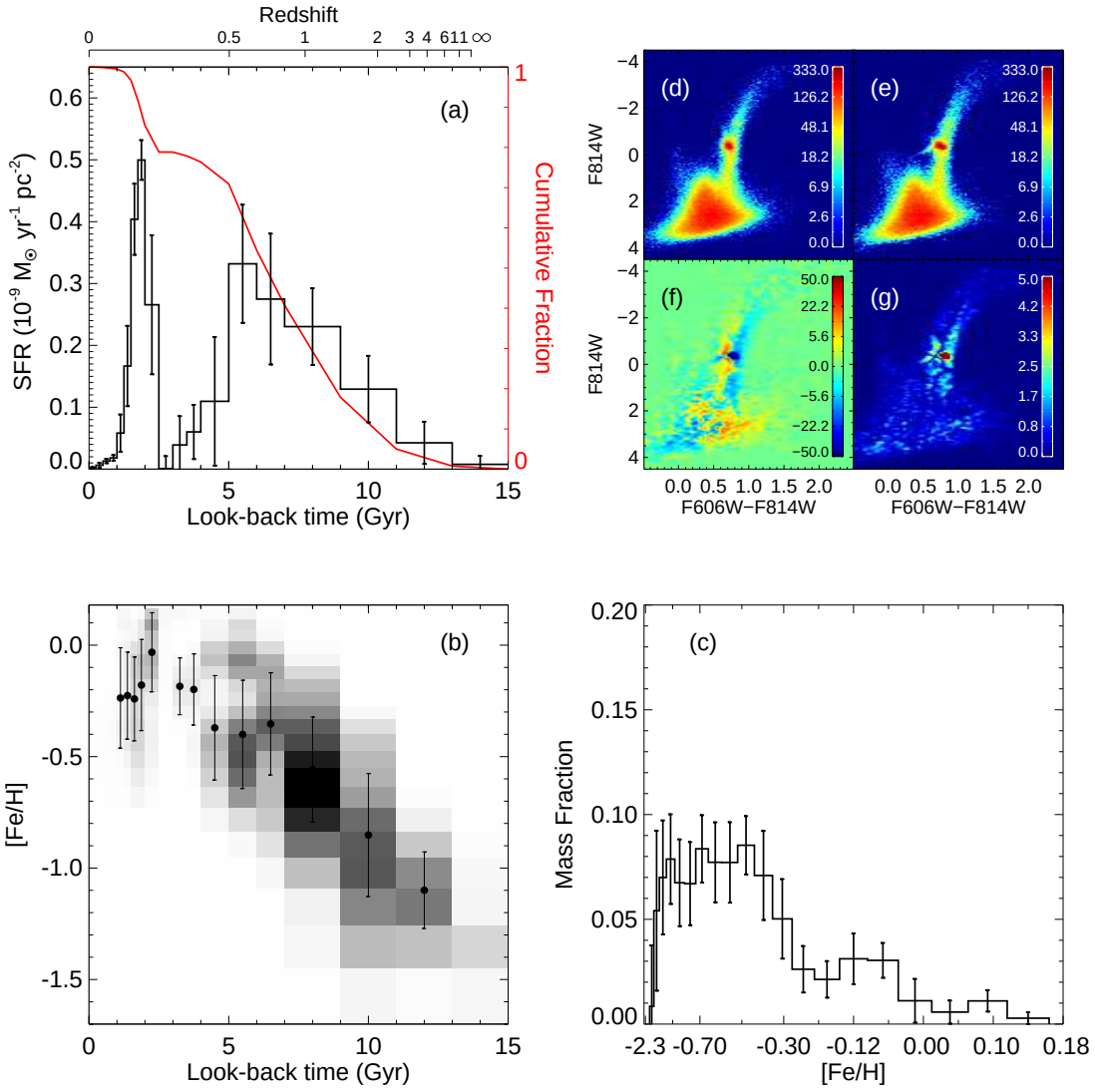

Figure 3. Best-fit SFH solution for the *Warp*. In the counter-clockwise direction, the panels show: (a) the SFR as a function of time, normalised to the area of the ACS field (deprojected for the M31 disc inclination), (b) the AMR, where the grayscale is proportional to the *stellar mass* formed in each bin, (c) the metallicity distribution of the mass of stars formed, (d)-(e) the Hess diagrams (i.e. star count per bin) of the observed and best-fit model CMDs, (f) the residuals, and (g) the significance of the residuals in Poisson σ. The cumulative mass fraction is shown in red in panel (a). The filled circles and error bars in panel (b) show the median metallicity and standard deviation in age bins representing at least 1 percent of the total mass of stars formed. See text for details.

from the BaSTI stellar evolution library (Pietrinferni et al. 2004) have been overplotted. The typical exposure times per pointing of $\sim$2 400 s in $F606W$ and $\sim$5 200 s in $F814W$ allowed us to obtain a signal-to-noise ratio $\geqslant 3$ over three magnitudes fainter than the horizontal-branch and red clump, i.e. comparable to the luminosity of a 12.5 Gyr old MSTO. The CMD of the *Warp*, shown in the middle panel of Figure 2, is one magnitude shallower than the CMD based on the full (i.e. 10 orbits) dataset for this field (see Figure 2 of Bernard et al. 2012); this has a slight effect on the accuracy of our SFHs, in particular at older ages (see Section 4.1).

A detailed comparative analysis of the CMDs, including a description of the main features and motivation for the classification as 'disc-like', 'stream-like', or 'composite', is given in Richardson et al. (2008). Specifically, they note that the stream-like fields harbor a more prominent blue HB and a wider RGB than the disc-like fields. These fields also have far fewer main-sequence (MS) stars younger than a few billion years compared to the disc-like fields. In particular, they lack the prominent over-density at $M_{606} - M_{F814} = 0.5$ and $M_{814} \sim 2$ corresponding to a 2 Gyr old population. The CMDs of the 'composite' fields, on the other hand, have properties which do not fit simply into either disc-like or stream-like categories.

3 STAR FORMATION HISTORIES

3.1 Method

To build on the results of Richardson et al. (2008), we have used the technique of synthetic CMD fitting to provide a more detailed and robust quantitative analysis of these fields. This involved fitting the observed data with synthetic CMDs to extract the linear combination of simple stellar populations (SSP) – i.e. each with

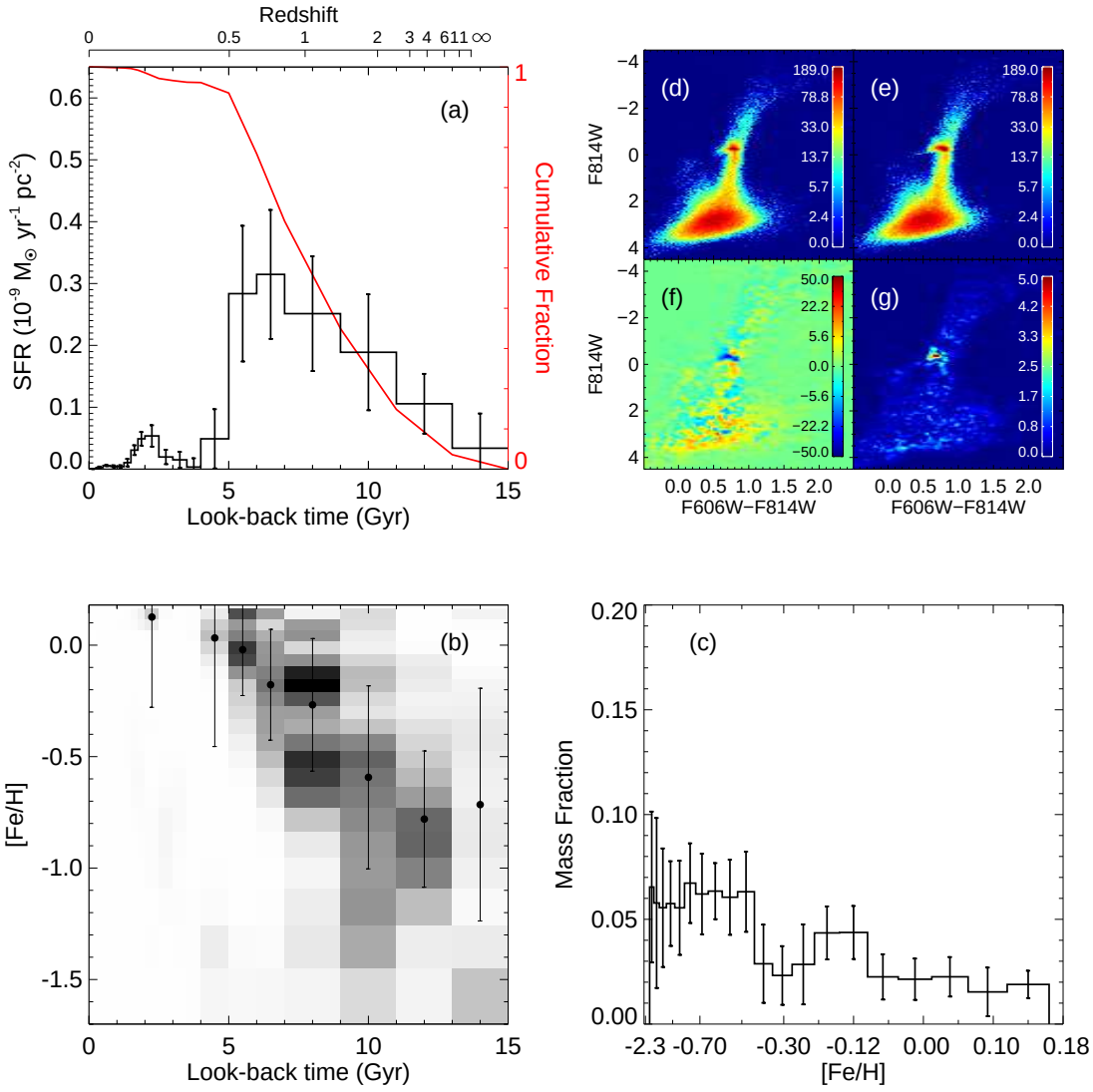

Figure 4. Same as Figure 3, but for the *Giant Stream*.

small ranges of age ($\leqslant$2 Gyr) and metallicity ($<$0.25 dex) – which provide the best fit; the amplitudes of which give the rates of star formation as a function of age and metallicity. When applied to sufficiently deep CMDs, this technique is very robust and has been shown to produce virtually indistinguishible results when using different algorithms (e.g. Monelli et al. 2010; Hidalgo et al. 2011).

We adopted the same methodology as in Bernard et al. (2012) and refer the interested reader to this paper for a detailed description. The method relies on the following programs: IAC-STAR (Aparicio & Gallart 2004) to generate the synthetic CMDs against which the observed CMD will be compared, IAC-POP (Aparicio & Hidalgo 2009) to find the combination of synthetic CMDs that best reproduce the observed CMD, and MINNIAC (Hidalgo et al. 2011) to produce the input files for, and process the output files from, IAC-POP, and to estimate the uncertainties.

The synthetic CMD from which we extracted the SSP CMDs is based on the BaSTI stellar evolution library (Pietrinferni et al. 2004); we note that using a different library only leads to small systematic differences of the order of $\sim$0.2 dex in metallicity, and $<$1 Gyr in age for ages older than $\sim$8 Gyr (e.g. Monelli et al. 2010; Bernard et al. 2012). The CMD, containing 10^7 stars, was generated with a constant star formation rate (SFR) over wide ranges of age and metallicity: 0 to 15 Gyr old and $0.0004 \leqslant Z \leqslant 0.03$ (i.e. $-1.7 \leqslant$ [Fe/H] $\leqslant 0.18$, assuming $Z_\odot = 0.0198$; Grevesse & Noels 1993). We adopted a Kroupa (2002) IMF, and assumed a binary fraction of 50 percent and a mass ratio $q > 0.5$ (see e.g. Kroupa, Tout & Gilmore 1991; Duquennoy & Mayor 1991; Gallart et al. 1999). Given the small size of the ACS field-of-view, the number of foreground and background contaminants in the regions of the CMD that are used for the SFH fitting is negligible; our model therefore does not attempt to account for foreground contamination. Finally, the incompleteness and photometric errors due to the observational effects have been simulated for each *HST* pointing based on the results of the corresponding artificial star tests.

The comparison between the observed and synthetic CMDs is performed using the number of stars in small colour-magnitude boxes. Due to both observational effects (e.g. signal-to-noise ratio)

Table 2. Results summary for the best-fit SFHs.

Field name	Type[a]	Stars ever formed		Stars still alive		Percentage of mass formed		
		$<$age$>^b$ (Gyr)	$<$[Fe/H]$>^b$	$<$age$>^b$ (Gyr)	$<$[Fe/H]$>^b$	<3 Gyr	<5 Gyr	>8 Gyr
Giant Stream	S	7.9	-0.33	7.1	-0.35	3.4 ± 0.9	6.5 ± 7.7	48.3 ± 6.5
Brown-stream	S	8.2	-0.35	7.1	-0.37	4.9 ± 1.8	10.2 ± 8.4	51.8 ± 6.1
Minor Axis	S	9.7	-0.41	8.2	-0.42	3.9 ± 4.1	7.1 ± 7.2	73.7 ± 11.0
EC1_field	S	8.4	-0.52	7.0	-0.47	6.2 ± 2.0	8.9 ± 6.8	55.7 ± 7.9
NE Shelf	S	7.5	-0.29	6.8	-0.40	3.7 ± 0.9	11.1 ± 5.7	43.0 ± 7.1
Average	S	8.3	-0.38	7.2	-0.40	4.4 ± 1.9	8.8 ± 7.2	54.5 ± 7.7
G1 Clump	D	6.6	-0.29	5.3	-0.37	13.0 ± 2.6	29.3 ± 4.2	30.5 ± 3.7
Warp	D	6.3	-0.43	4.6	-0.36	21.1 ± 1.8	29.1 ± 3.6	29.4 ± 2.1
Claw	D	8.3	-0.29	6.6	-0.32	8.0 ± 2.3	19.1 ± 4.3	52.8 ± 4.1
N Spur	D	6.8	-0.20	5.6	-0.28	10.7 ± 1.8	25.7 ± 3.2	34.1 ± 3.6
NE Clump	D	7.0	-0.32	6.0	-0.40	7.3 ± 2.1	22.4 ± 4.6	38.0 ± 5.7
Average	D	7.0	-0.31	5.6	-0.35	12.0 ± 2.1	25.1 ± 4.0	37.0 ± 3.8
GC6_field	C	8.2	-0.24	5.8	-0.26	8.9 ± 2.8	21.8 ± 3.1	52.0 ± 4.3
NGC205 Loop	C	8.5	-0.37	6.5	-0.39	8.8 ± 3.6	18.1 ± 5.1	57.0 ± 5.6
Brown-disk	C	7.6	-0.27	6.6	-0.32	5.9 ± 1.9	14.7 ± 5.1	44.8 ± 5.2
Brown-spheroid	C	8.8	-0.53	7.6	-0.50	4.7 ± 1.6	7.6 ± 6.0	59.5 ± 6.2
Average	C	8.3	-0.35	6.6	-0.37	7.1 ± 2.5	15.5 ± 4.8	53.4 ± 5.4

[a] S: stream-like; D: disc-like; C: composite.
[b] Median age and metallicity.

and theoretical uncertainties in stellar evolution models, some areas of the CMDs are more reliable than others. We limit the comparison to a number of specific areas (called 'bundles'; Aparicio & Hidalgo 2009, see also Monelli et al. 2010) shown as black solid lines in the right panel of Figure 2. The bundles are then divided uniformly into small boxes, with a size depending on the density of stars and reliability of the stellar evolution models: these are shown by thin blue lines in the right panel of Figure 2. Since every box carries the same weight, the number of boxes in a bundle determines the weight that the region has for the derived SFH. In our analysis, the main bundle covers the MS and sub-giant branch, where the models are less affected by the uncertainties in the input physics; this bundle is divided into 0.1×0.06 mag boxes. The other three bundles we use lie at the base, on the red side, and over the tip of the RGB and serve to provide mild constraints on the metallicity. Since the models for these evolved phases are more uncertain, and the differences between stellar libraries more important (Gallart, Zoccali & Aparicio 2005), we used significantly larger boxes; 0.1×0.5 for the former, and 0.3×0.5 for the latter two. This yields a total number of ~ 530 boxes.

The best-fit SFH is determined by finding the amplitudes of the linear combination of SSP CMDs which best match the observed CMD. The number of observed stars, and artificial stars from each SSP, counted in each CMD box, serves as the only input to IAC-POP. No a priori AMR, or constraint thereon, is adopted: IAC-POP solves for both ages and metallicities simultaneously within the age-metallicity space covered by our SSPs. The goodness of the coefficients in the linear combination is measured through the modified χ^2 statistic of Mighell (1999), which IAC-POP minimizes using a genetic algorithm. These coefficients are directly proportional to the star formation rate of their corresponding SSPs.

To sample the vast parameter space, the χ^2 minimization is repeated several hundred times for each field after shifting the bin sampling in both colour–magnitude and age–metallicity space. In addition, the observed CMD is shifted with respect to the synthetic CMDs in order to account for uncertainties in photometric zero-points, distance, and mean reddening.

Finally, the uncertainties on the SFRs were estimated following the prescriptions of Hidalgo et al. (2011, see also Aparicio & Hidalgo 2009). The total uncertainties are assumed to be a combination (in quadrature) of the uncertainties due to the effect of binning in the colour–magnitude and age–metallicity planes, and those due to the effect of statistical sampling in the observed CMD.

3.2 Results

Our results reveal quantitative differences in the derived SFHs that fully support the inferences made by Richardson et al. (2008) on the basis of a comparative analysis of CMD morphology alone. Rather than showing the detailed best-fit solutions for each of the fourteen fields, we present solutions for an illustrative disc-like and a stream-like field, as well as the main features in synthesized form for all the fields; the individual solutions for the other fields are given in the Appendix. We also summarize the results in Table 2: for each field, we list the median age and metallicity of all the stars ever formed, as well as the percentage of the total stellar mass formed in the last 3 Gyr and 5 Gyr ($z \sim 0.5$), and the mass already in place by $z \sim 1$ (8 Gyr ago) according to the best-fit solutions. To allow comparison with observations, we include the median age and metallicity of the stars that are still alive today (i.e. excluding the stars that have evolved to become white dwarfs or supernovae) in columns 5 and 6. We also show the average quantities for each field type.

Figures 3 and 4 show the best-fit solutions for a disc-like field (the *Warp*) and a stream-like field (the *Giant Stream*), respectively. In the counter-clockwise direction, the panels show: the evolution of the SFR (a) and metallicity (b) as a function of look-back time;

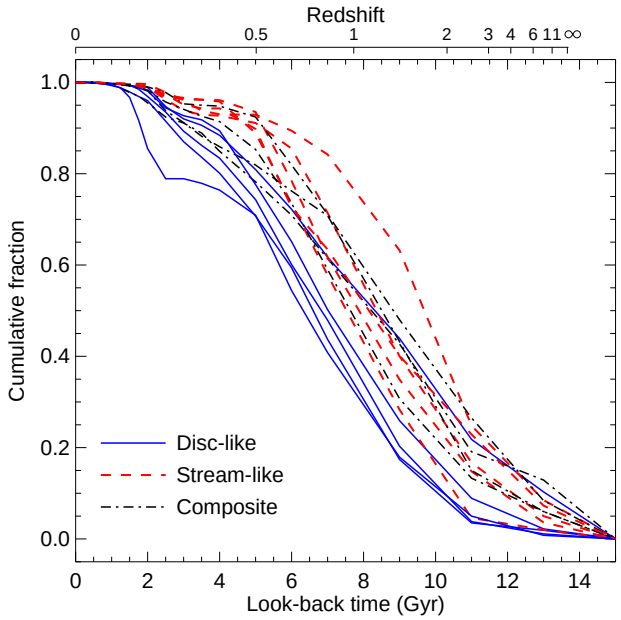

Figure 5. Cumulative mass distributions for our 14 fields showing the fraction of stellar mass formed in each of the substructure fields as a function of look-back time. The disc-like, stream-like, and composite fields are represented by solid blue lines, red dashed lines, and black dotted lines, respectively. The disc-like fields can be seen to be systematically younger, on average, than the other fields.

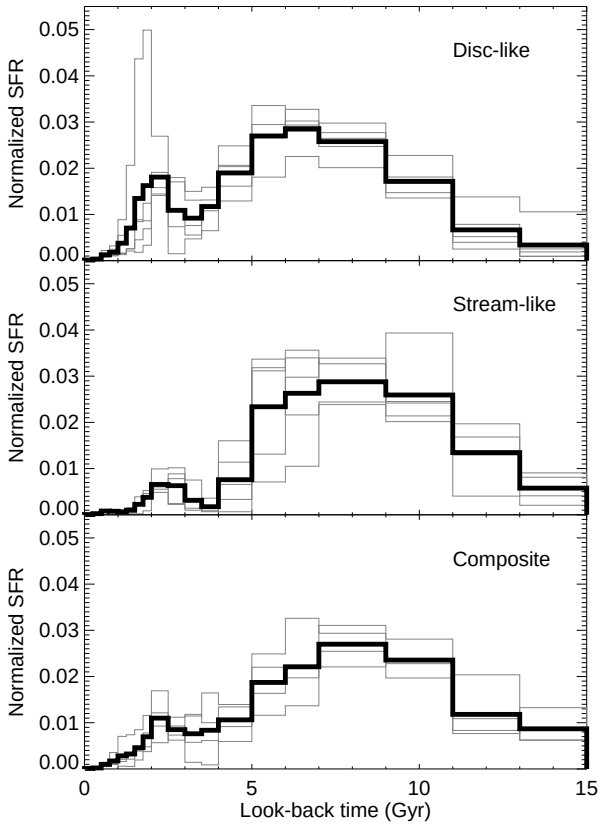

Figure 6. The SFH of the disc-like (top), stream-like (middle), and composite (bottom) fields, normalised to the total mass of stars formed in each field, where the individual fields are shown with different line styles. The thick gray lines represent the average of the normalized SFHs.

(c) the metallicity distribution of the mass of stars formed; (d)-(e) the Hess diagrams of the observed and best-fit model CMDs, with a logarithmic stretch to bring out fainter features; (f) the residual differences between the two, in the sense observed−model; and (g) the absolute residual difference normalized by Poisson statistics in each bin. The redshift scale shown on panel (a) was constructed assuming the WMAP7 cosmological parameters from Jarosik et al. (2011), namely $H_0 = 71.0$ km s^{-1} Mpc^{-1}, $\Omega_\Lambda = 0.73$ and $\Omega_\mathrm{M} = 0.27$.

The comparison of panels (d) and (e) in these figures shows that the best-fit SFH solutions reproduce the data very well. The panels showing the residuals of the fits indicate where the models struggle to replicate the data – significant deviations of the model from the data appear as strong coherent residuals. The RC is the only phase of stellar evolution that the algorithm has consistently failed to fit well due to known limitations of the current stellar evolution models (Gallart, Zoccali & Aparicio 2005). As discussed previously, this is the reason why this region of the CMD has not been included in the SFH calculations, and therefore carries no weight in our final solution. Otherwise the patterns of residuals display no significant systematic disparities between the models and the data; while the model RGB close to the tip is sometimes wider than the observed RGB, we recall here that the theoretical models of this evolutionary phase are less reliable (e.g. Gallart, Zoccali & Aparicio 2005; Cassisi 2013), hence their low weight in the SFH calculations. Besides, none of the fields have residuals in this part of the CMD with significance larger than $\sim$1-σ.

Our homogeneous analysis of the best-fit SFH results demonstrate a dichotomy in the nature of the stellar substructure in M31's inner halo, as first pointed out by Richardson et al. (2008). The main differences between the two types of fields are the typically older median ages of the stream-like fields, as well as their more rapid chemical enrichment. The former is illustrated in Figure 5, where the cumulative mass fractions of all fourteen fields are shown together. It shows that the disc-like fields, represented by solid blue lines, formed very few stars before about 10 Gyr ago ($z \sim 2$), and have a median age of $\sim$7 Gyr. Instead, star formation started very early in the stream-like fields but decreased to residual levels by 4–5 Gyr ago; their median age is on average 1.5 Gyr older. As expected from their CMD morphologies, the fields flagged as composite in Richardson et al. (2008) have properties intermediate between the other two: an early onset of star formation like the stream-like fields, yet substantial star formation in the past 5 Gyr (see below).

Figure 6 shows the SFR as a function of time for all the fields, separated by field type and normalized to the total mass of stars formed in each field, as well as the mean SFR for each type. In Bernard et al. (2012), we found that the *Warp* underwent a brief but strong burst of star formation $\sim$2 Gyr ago, which we suggested could have been triggered by the pericentric passage of M33 at that time. Interestingly, Figure 6 shows that *all* our fields show an enhancement in the star formation rate at this time, although the relative strength of this burst seems stronger in the disc-like fields. We note that this young population is unlikely to be due to blue stragglers, since it represents a significant fraction of the total mass of stars formed (between 5 and 25 percent). Moreover, these stars have a higher metallicity than expected from merging or mass-transfer in old, metal-poor stars, the currently-favoured scenarios for produc-

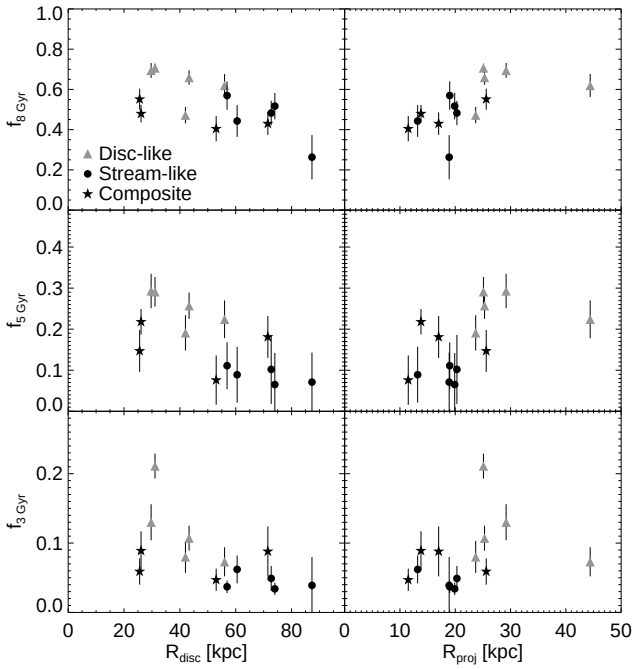

Figure 7. Fraction of stars formed in the last 8 Gyr (top), 5 Gyr (middle), and 3 Gyr (bottom) as a function of de-projected (left) and projected (right) radius. The disc-like, stream-like, and composite fields are represented by gray triangles, black filled circles, and black stars, respectively. Note the differing vertical scales.

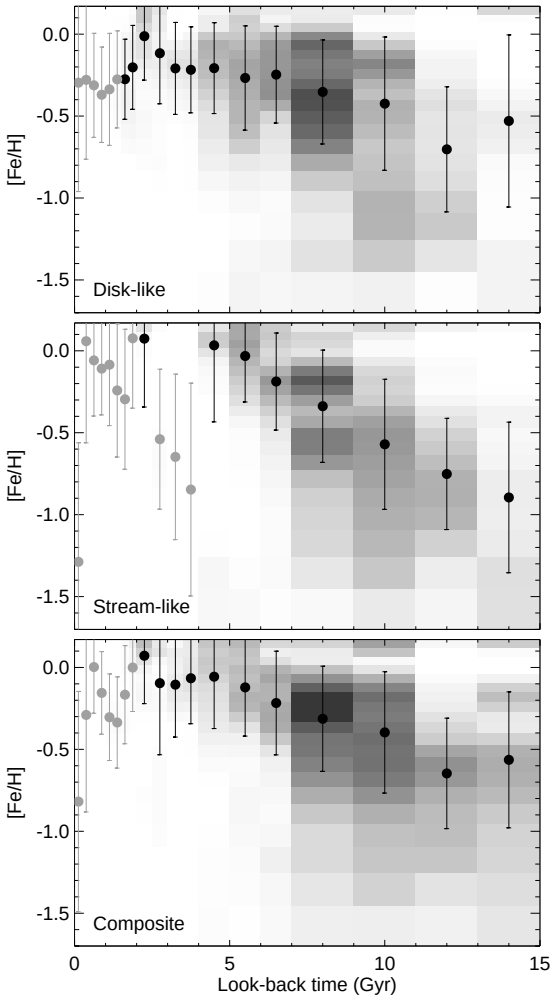

Figure 8. The AMR of the disc-like (top), stream-like (middle), and composite (bottom) fields, where the grayscale is proportional to the stellar mass formed in each bin. The AMRs of the individual fields were weighted by the total mass of stars formed in each. Filled circles mark the median metallicity in each age bin; gray symbols were used for age bins representing less than 1 percent of the total mass, where the metallicity is therefore less reliable. Error bars show the standard deviation in each bin.

ing blue stragglers. We discuss the implications of detecting this apparently ubiquitous burst in Section 4.3.

Figure 7 shows the fraction of the total stellar mass formed in the last 8 Gyr ($z \sim 1$, top), 5 Gyr ($z \sim 0.5$, middle), and 3 Gyr (bottom) as a function of the deprojected (left) and projected (right) radius from the centre of M31. The disc-like, stream-like, and composite fields are represented by gray triangles, dark gray circles, and black stars, respectively. The trend in the top left panel indicates that the outermost fields had a significant fraction of the mass already in place by $z \sim 1$, while the fields closer to the centre of M31 are on average younger. However, this may just reflect the complicated merger history of this galaxy rather than imply an outside-in formation of the outer disc and inner halo. In addition, the deprojected distance is based on the assumption that all the fields are located in the same plane as the M31 disc, which is clearly not always the case (e.g. McConnachie et al. 2003). The top right panel shows the reverse trend – i.e. younger populations at larger radii – but this simply reflects the locations of the fields probed: the disc-like (stream-like) fields tend to be located close to the major (minor) axis, thus appearing farther from (closer to) the centre of M31.

Indeed the middle panels of Figure 7 indicate that the disc-like fields have a systematically larger fraction of young stars than the stream-like fields: disc-like fields formed ∼25 percent of their stellar mass in the last 5 Gyr while stream-like fields formed only about 9 percent in the same time period. Similarly, in the past 3 Gyr, the disc-like fields formed ∼12 percent of their total stellar mass, compared to only 4 percent for the stream-like fields. Overall, Figure 7 shows that there are no strong radial gradients in the median age of the stellar population at these galactocentric distances.

The other significant difference between the disc-like and stream-like substructure fields is evident in their AMRs. Figures 3 and 4 show that while the metallicity evolution is rather well constrained in both cases, it proceeded at a different rate. The metallicity of the *Giant Stream* covers the whole range spanned by the isochrone set, and reached the maximum metallicity of the grid roughly 5 Gyr ago. On the other hand, the metallicity evolution was slower in the *Warp*, lacking a population of the most metal-poor stars and reaching solar metallicity only ∼2 Gyr ago.

The AMRs of the other stream-like fields are basically indistinguishable from that of the *Giant Stream* field, suggesting a high degree of chemical homogeneity in the stream progenitor. While the AMRs of the disc-like fields show somewhat more variation, they share the same features as the AMR of the *Warp* – i.e. generally lacking the two extremes of the metallicity range, leading to a milder metal enrichment. Some of these fields are located on rather diffuse and complex structures in the outskirts of M31, so the complexity of their AMRs may be a consequence of the superposition of substructure along the line of sight.

Figure 8 presents the weighted mean AMRs of the disc-like, stream-like, and composite fields, where the median metallicity and

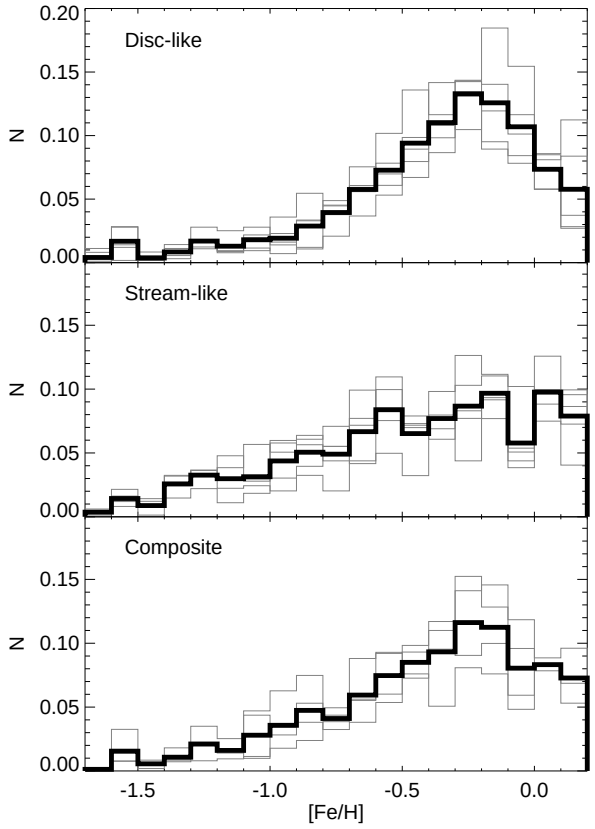

Figure 9. The MDFs of stars brighter than $M_{814} < -1.5$ that are still alive today, according to our best-fit SFHs, in the disc-like (top), stream-like (middle), and composite (bottom) fields. These are normalized to the total mass of stars formed in each field. The line styles are as in Figure 6.

standard deviation in each age bin are shown as filled circles and error bars. The difference in chemical enrichment histories persists here. The top panel shows that the metallicity of the disc-like fields increased from [Fe/H]~ -0.7 to solar metallicity $\sim$2 Gyr ago. The decline in global metallicity following the recent burst was already observed in our SFH of the *Warp* obtained from the full depth data, where we have shown that it is not an artifact of the method (Bernard et al. 2012, see also Brown et al. 2006). In contrast, the AMR of the stream-like fields reveals a more rapid chemical enrichment, from [Fe/H]~ -1 to solar metallicity before 5 Gyr ago.

The difference in AMRs is also reflected in the predicted present-day metallicity distribution functions (MDFs). Figure 9 shows the MDFs of stars brighter than $M_{814} < -1.5$ (i.e. F814W ~ 23[3]) *that are still alive today* according to the best-fit SFHs for each field. The MDFs were obtained by selecting the bright stars from the solution CMDs (panel (e) in, e.g. Figure 3), for which we know the individual age and metallicity. We find that the MDF of the disc-like fields has a bell-shape peaking at [Fe/H]~ -0.2, with very few low-metallicity stars. On the other hand, the stream-like MDF is significantly flatter, and although increases smoothly it has no clear peak. The fact that considerable stars are present in the highest metallicity bin available in our models may indicate that even more metal-rich stars are present in the GSS.

Finally, the 'composite' fields display a variety of behaviours which do not fit easily into either disc-like or stream-like categories, consistent with them being a complicated mixture of both. The SFH of the *Brown-spheroid* field is more akin to those of the stream-like fields, while the three other composite fields more resemble the disc-like fields. Their SFRs (Figure 6) and MDFs (Figure 9) are intermediate between those of the stream-like and disc-like fields, while their AMRs are closer to the latter fields. It is likely that these fields sample regions where material stripped from the GSS progenitor is mixed together with material from the perturbed thin disc, or that the GSS progenitor contained gradients in its stellar populations. For example, if the progenitor was a disc galaxy (e.g. Fardal et al. 2008) it would have shed different populations (corresponding to mixtures of bulge, disc and halo stars) as it dissolved in its orbit around M31. We do not discuss these fields further and instead focus on the prominent differences between disc-like and stream-like fields and what they imply for the origin and nature of the underlying populations.

4 DISCUSSION AND INTERPRETATION

4.1 Comparison with literature results

The average metallicities of all the fields, shown in Table 2, lie in the range $-0.5 \lesssim$ [Fe/H] $\lesssim -0.3$. This is in good agreement with the previous photometric and spectroscopic studies probing the outer disc and inner halo of M31, as well as the GSS (e.g. Mould & Kristian 1986; Durrell, Harris & Pritchet 1994; Holland, Fahlman & Richer 1996; Ferguson & Johnson 2001; Bellazzini et al. 2003; Ferguson et al. 2005; Brown et al. 2006; Kalirai et al. 2006; Gilbert et al. 2009; Fardal et al. 2012; Ibata et al. 2014).

There are a few papers in the literature in which the SFH of a subset of the fields presented here was calculated using similar methods. Using STARFISH (Harris & Zaritsky 2001), Brown et al. (2006) fit the SFHs of the *Brown-stream*, *Brown-spheroid*, and *Brown-disk*, at their full depth, $\sim$1.5 mag deeper than in this analysis and consisting of over 32 *HST* orbits per pointing. We have analysed only a subset of these data in order to match the depth of our other HST/ACS fields and thus allow a homogeneous comparison. The additional depth used in the Brown et al. analysis had the advantage of allowing them to reach the oldest MSTO, enabling a probe of the earliest stages of star formation with more detail and accuracy than we have here. Although following a similar synthetic CMD technique to the one described here, Brown et al. (2006) used the Victoria-Regina isochrones (VandenBerg, Bergbusch & Dowler 2006) with a larger range of metallicities ($-2.2 \leqslant$ [Fe/H] $\leqslant +0.5$), so minor systematic differences are expected.

It is difficult to quantitatively compare their results to ours because they only present qualitative AMRs (similar to our panel (b) in Figures 3 and 4), without the corresponding histograms showing the evolution of the SFR with time, the metallicity distribution, and their associated uncertainties. However, the qualitative agreement between their AMRs (their Figures 9, 13 and 18) and ours is excellent, especially given the different libraries used and the range of metallicities available in the isochrone sets. They found that the majority of stellar mass in the *Brown-stream* and *Brown-spheroid* fields formed between 5 – 14 Gyr with a considerable range of

[3] This is roughly the magnitude limit at which spectroscopy of individual stars can be carried out with the current generation of 8-m telescopes and instruments.

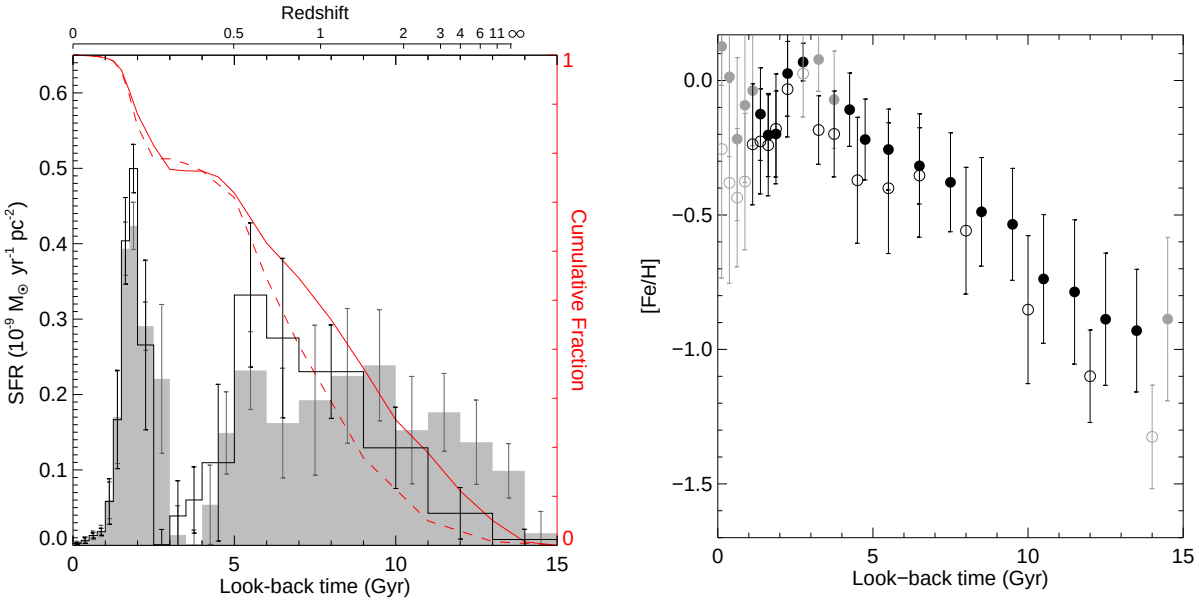

Figure 10. Comparison of the *Warp* SFH obtained with the deep dataset in Bernard et al. (2012) and with the shallower data in this work (see text for details). *Left*: SFR as a function of time for the deep (filled gray histogram) and shallower (black histogram) datasets. The solid (dashed) red line shows the cumulative mass fraction of the deep (shallower) dataset. *Right*: Median metallicity as a function of time. Filled and open circles represent the deep and shallower data, respectively. As in Figure 8, gray symbols denote age bins that are less reliable due to the low SFR. Error bars show the standard deviation in each bin.

metallicities and rapid chemical enrichment. All three of the fields they analysed showed low amplitude star formation within the last 4 Gyr, while their *Brown-disk* field was found to be dominated by younger (4 to 8 Gyr old) populations and lacked metal-poor stars. These findings mirror the results we have obtained here from an analysis of shallower versions of their datasets.

Secondly, Faria et al. (2007) also used StarFISH to model the MS, RC and RGB of the *G1 Clump* and visually compared the simulated luminosity functions and distribution of stars on the CMD to the observed data. They concluded that the bulk of the mass in the *G1 Clump* was in place more than 6 Gyr ago but that 10 percent of the mass was formed in the last 2 Gyr. Based on Table 2, we find that ∼71 percent of the mass was in place by 5 Gyr ago and ∼13 percent formed in the last 3 Gyr. Faria et al. (2007) also find a relatively high mean metallicity of [Fe/H] = −0.4, a large metallicity dispersion of $\gtrsim$ 0.5 dex and little evidence for chemical evolution. These results are in very good agreement with those presented here.

Finally, in Bernard et al. (2012) we presented the SFH of the *Warp* based on the full dataset (i.e. 10 orbits vs. the 3 used here), reaching about one magnitude deeper. The higher signal-to-noise ratio at the magnitude of the MSTO and larger number of stars in the CMD allowed us to use a finer grid in age and metallicity (see Figure 6 in Bernard et al. 2012). The comparison of the results is presented in Figure 10. It shows that the SFR and AMR obtained in each case are in very good agreement, with most discrepancies smaller than 1-σ. We note that the SFH obtained from the shallower data appears to be slightly offset toward younger ages (∼0.5 Gyr on average) and lower metallicities (mean Δ[Fe/H] = 0.12); however, these offsets are smaller than the ones we found when comparing the SFHs obtained with the BaSTI and Padova (Girardi et al. 2000) libraries on the deep dataset (Appendix A in Bernard et al. 2012, see also Barker et al. 2011), and therefore are not the dominant source of uncertainties. The main drawback of the shallower data is that the details of the SFH at older ages are less reliable (see also Weisz et al. 2014). In particular, the AMR is not as well constrained, leading to higher uncertainties on the age of stars beyond $z \sim 1$, and the median age is found to be slightly younger (∼6.5 Gyr) than from the deeper data (∼7.5 Gyr). According to the 50 percent completeness limits, the *Warp* is one of the shallower fields analyzed here – the fourth out of 14. We therefore expect that the limitations due to the depth of the photometry will be similar or less significant in most of the fields.

4.2 Constraints on the SFH of the Giant Stream Progenitor

The GSS was discovered in the INT/WFC wide-field panoramic survey of M31 over a decade ago (Ibata et al. 2001), and is falling in from the far side of M31 (McConnachie et al. 2003). It has been modeled with some success by various groups (e.g. Ibata et al. 2004; Font et al. 2006; Fardal et al. 2007; Mori & Rich 2008; Sadoun, Mohayaee, & Colin 2014). These N-body simulations suggest that the stream and associated shelves are the tidal debris of a progenitor with a total mass of a few $10^9 - 10^{10} M_\odot$ that fell in to M31 in the last billion years. It is inferred to have come in on a highly radial orbit, and have wrapped around the inner galaxy at least twice. However, the exact nature of the satellite involved in this substantial accretion event remains a mystery. Kinematical constraints rule out both M 32 and NGC 205 as candidates and simulations predict that the remnant should be located in the northeast half of the M31 disc (Ibata et al. 2004; Fardal et al. 2013). To date, no obvious source has been found in this region with either the INT/WFC survey, nor in the deeper *Pan-Andromeda Archaeological Survey* (McConnachie et al. 2009).

As the GSS progenitor fell towards M31, long tidal tails are expected to be produced, both leading and trailing the progenitor core. Through comparison to the N-body simulation of Fardal et al. (2007), Richardson et al. (2008) demonstrated that the *Giant Stream* and *Brown-stream* fields directly probe the trailing stream while the *NE Shelf*, *EC1_field* and *Minor Axis* fields probe

wraps of the leading stream. The results of the SFH fits allow us to place new constraints on the nature of the GSS progenitor. Perhaps the most interesting feature of the best-fit SFHs of all the stream-like fields is the ubiquitous spread of metallicity ($\gtrsim$ 1.5 dex) among the older populations, as expected from the significantly redder RGB than in the smooth halo component (Ferguson et al. 2002; Ibata et al. 2014). We find that these fields enriched from ~ -1.5 dex to at least solar metallicity within $\sim$8 Gyr of evolution. Such rapid enrichment is characteristic of early-type dwarf galaxies and the bulges of spirals (e.g. Sagittarius dwarf: Siegel et al. 2007). Interestingly, some properties of the observed stream – in particular the asymmetric distribution of stars along the stream cross section – are better reproduced in N-body models in which the progenitor possessed a rotating disc (e.g. Fardal et al. 2008; Sadoun, Mohayaee, & Colin 2014). The homogeneous AMRs we have derived for the stream-like fields suggest that either there were no strong population gradients in the progenitor or that the inner halo is littered with material from only the central regions of the progenitor, rather than the metal-poor stars which might dominate its outskirts.

Another common feature of all stream-like fields is the sharp decrease in star formation $\sim$5 Gyr ago, also seen by Brown et al. (2006) in the field they analysed. Additionally, Ferguson et al. (2002) noted the lack of intermediate-age AGB stars in the substructure associated with the stream. This quenching of star formation is interesting, as it may indicate when the progenitor first entered the halo of M31. Ram pressure by hot gas in the corona of large galaxies is well known to strip smaller galaxies of their gas and lead to the cessation of star formation (e.g. Mayer et al. 2006). Indeed, a detailed comparison of the stellar and gaseous distributions around M31 found no H I associated with the GSS, indicating that whatever gas the progenitor had was lost a long time ago (Lewis et al. 2013). The results from our SFH fits may help to tailor future the N-body simulations of the GSS progenitor's orbital evolution around M31.

4.3 Ubiquity of the 2-Gyr-old burst: evidence for disc heating?

In Bernard et al. (2012), we demonstrated that the *Warp* field underwent a strong burst of star formation $\sim$2 Gyr ago that lasted about 1.5 Gyr. Prior to this, there was a rapid decline in the star formation rate and almost a complete lull in activity for the preceding Gyr. In that analysis, we interpreted this burst as a consequence of the close passage of M33, which self-consistent N-body modeling indicated should have occured around the time of the onset of the burst (McConnachie et al. 2009). Such an interaction and subsequent burst are further supported by the overabundance of 2 Gyr old star clusters clusters (Fan, de Grijs, & Zhou 2010) and planetary nebulae (Balick et al. 2013). However, our interpretation relied on the SFH of a single pencil-beam pointing in the outer disc of M31.

The SFH derivations presented here enable us to strengthen the argument for a large-scale burst of star formation in M31 which took place $\sim$ 2 Gyr ago. All 14 fields analysed in this work show an enhancement of the star formation rate at this epoch, regardless of their location. Considerable field-to-field variations exist in the intensity of this enhancement, however. After the *Warp*, the *NSpur* and *GC6_field* fields exhibit the next most intense bursts of star formation, both of which reach peak intensities that are roughly half of that seen in the *Warp*. It is notable that the *NSpur* is located at the opposite end of the M31 disc from the *Warp* (i.e. about 50 kpc away). The detection of the burst over such a large area, as well as in the outer disc of M33 (see Bernard et al. 2012, and references therein), lends further credence to the idea of a disc-wide burst triggered by a close passage.

The large intensity of star formation during the burst in the *Warp* and *NSpur* fields is most likely due to their location within the thin disc of M31. However, the detection of the 2 Gyr old burst in the other fields, in particular those at locations associated with large deprojected radii, is more puzzling. Deep 21 cm observations show that high column density neutral hydrogen in M31 is largely confined within the inner 2° (27 kpc, shown as the inner ellipse in Figure 1; Braun et al. 2009; Chemin, Carignan, & Foster 2009), while the molecular hydrogen – as traced by the carbon monoxide lines – is even less extended ($R_{disc} \lesssim$ 16 kpc; Nieten et al. 2006). Unless the gas distribution in M31 was significantly more extended in the past, it seems unlikely that star formation could have occured *in situ* in our outermost fields. Instead, it seems more plausible that the young populations in these fields originate in material that has been recently kicked-out from the thin disc. This idea was first raised by Richardson et al. (2008) who noticed the similarity between some inner halo CMDs and the stellar populations in the thin disc of M31. There has been mounting evidence over the past two decades of the disruptive effects of minor mergers and continued interactions with dark matter sub-halos to heat, thicken and perturb MW-like stellar discs, providing a method capable of producing such low-latitude substructure while preserving the global thin disc structure (e.g. Quinn, Hernquist & Fullagar 1993; Walker, Mihos & Hernquist 1996; Velazquez & White 1999; Gauthier, Dubinski & Widrow 2006; Kazantzidis et al. 2009; Purcell, Bullock, & Kazantzidis 2010; Tissera et al. 2013). The fact that some of the M31 substructure exhibits disc-like kinematics, even at radii of $\sim$70 kpc, certainly supports the idea that the disc has undergone significant disruption (Ibata et al. 2005). Additionally, kinematic evidence for the presence of heated disc stars in the halo has recently been found in both the Milky Way (Sheffield et al. 2012) and M31 (Dorman et al. 2013).

Hence, we favour an interpretation where the young populations were formed at smaller galactocentric distances, where the molecular gas density was sufficient to support star formation, and were subsequently displaced to their present locations through the rearrangement of material following a minor merger. There is ample evidence that M31 has had a rich interaction and merger history (e.g. Ibata et al. 2001; McConnachie et al. 2009; Gilbert et al. 2009; Bate et al. 2013), with the most significant recent event being the accretion of the GSS progenitor. Recent modelling work suggests the last pericentric passage of the progenitor took place 760 ± 50 Myr ago (Fardal et al. 2013). This event may have had enough clout to heat and perturb the thin disc to redistribute disc stars of all ages to large distances, and is thus consistent with the fact that a population of $\sim$ 2 Gyr stars is present in all fields, regardless of their radial distance or position relative to the main gas disc.

5 CONCLUSIONS

We have presented the quantitative SFHs of 14 deep *HST/ACS* fields which probe different stellar substructures in the outer disc and inner halo of M31. The SFHs we derive reinforce both the results obtained from a morphological comparison of their CMDs by Richardson et al. (2008), and the results from the analysis of a

much deeper CMD of the *Warp* field by Bernard et al. (2012). In particular, we find that:

- the classification of the fields into two primary categories – 'stream-like' and 'disc-like' – still holds when examining their quantitative SFHs. We find that disc-like fields formed most of their mass ($\sim$65 percent) since $z \sim 1$, yielding a median age of 7 Gyr, with one quarter of the stellar mass formed since 5 Gyr ago. The stream-like fields, on the other hand, are on average 1.5 Gyr older and have formed $\lesssim$10 percent of their stellar mass within the last 5 Gyr.
- the stream-like fields are characterised by an AMR showing rapid chemical enrichment from [Fe/H]~ -1.7 to roughly solar metallicity by $z = 1$, suggesting an early-type progenitor such as a dwarf elliptical galaxy or a bulge.
- the burst of star formation about 2 Gyr ago, first identified in our previous analysis of the southern warp as well as in the outer disc of M33, is detected in *all* the fields studied here, albeit with varying intensity. The widespread nature of this event, combined with the fact it coincides with predictions for the last pericentric passage of M33, lends strong support to the interaction hypothesis.
- the presence of $\sim$2 Gyr old stars over 50 kpc from the centre of M31 – or 10 kpc above the disc, i.e. well beyond the current extent of both the molecular and neutral hydrogen discs – is most easily explained if this population has been scattered from the thin disc during a recent encounter. The close interaction between M31 and M33, combined with the recent impact of the GSS progenitor, add weight to the idea that repeated interactions between M31 and its massive satellites could have enough clout to heat and perturb the thin disc to redistribute some disc material into the complex substructure we see today.

ACKNOWLEDGMENTS

This work was supported by a Marie Curie Excellence Grant from the European Commission under contract MCEXT-CT-2005-025869 and a consolidated grant from STFC. SLH and AA acknowledge support by the IAC (grant 310394) and the Science and Innovation Ministry of Spain (grants AYA2007-3E3507 and AYA2010-16717). GFL thanks the Australian Research Council for support through his Future Fellowship (FT100100268) and Discovery Project (DP110100678).

REFERENCES

Aparicio A., Gallart C., 2004, AJ, 128, 1465
Aparicio A., Hidalgo S. L., 2009, AJ, 138, 558
Barker M. K., Ferguson A. M. N., Cole A. A., Ibata R., Irwin M., Lewis G. F., Smecker-Hane T. A., Tanvir N. R., 2011, MNRAS, 410, 504
Balick B., Kwitter K., Corradi R., Henry R., 2013, ApJ, 774, 3
Barmby P., McLaughlin D. E., Harris W. E., Harris G. L. H., Forbes D. A., 2007, AJ, 133, 2764
Bate N. F., et al., 2013, MNRAS, 437, 3362
Bedin L. R., 2010 (astro-ph/1011.0436)
Bellazzini M., Cacciari C., Federici L., Fusi Pecci F., Rich M., 2003, A&A, 405, 867
Bernard E. J., et al., 2012, MNRAS, 420, 2625
Braun R., Thilker D. A., Walterbos R. A. M., Corbelli E., 2009, ApJ, 695, 937
Brinks E., Burton W. B., 1984, A&A, 141, 195
Brown T. M., Ferguson H. C., Smith E., Kimble R. A., Sweigart A. V., Renzini A., Rich R. M., VandenBerg D. A., 2003, ApJ, 592, L17
Brown T. M., Smith E., Ferguson H. C., Rich R. M., Guhathakurta P., Renzini A., Sweigart A. V., Kimble R. A., 2006, ApJ, 652, 323
Cassisi S., 2013, in Charbonnel C., Lebreton Y., Valls-Gabaud D., eds, 23rd Evry Schatzman School on Stellar Astrophysics: "The Ages of Stars". EDP Sciences: Les Ulis, preprint (astro-ph/1312.5968)
Chemin L., Carignan C., Foster T., 2009, ApJ, 705, 1395
Cignoni M., Degl'Innocenti S., Prada Moroni P. G., Shore S. N., 2006, A&A, 459, 783
Dalcanton J. J., et al., 2012, ApJS, 200, 18
Davidge T. J., 2000, PASP, 112, 1177
Dorman C. E., et al., 2013, ApJ, 779, 103
Duquennoy A., Mayor M., 1991, A&A, 248, 485
Durrell P. R., Harris W. E., Pritchet C. J., 1994, AJ, 108, 2114
Fan Z., de Grijs R., Zhou X., 2010, ApJ, 725, 200
Fardal M. A., Babul A., Guhathakurta P., Gilbert K. M., Dodge C., 2008, ApJ, 682, L33
Fardal M. A., Guhathakurta P., Babul A., McConnachie A. W., 2007, MNRAS, 380, 15
Fardal M. A., et al., 2012, MNRAS, 423, 3134
Fardal M. A., et al., 2013, MNRAS, 434, 2779
Faria D., Johnson R. A., Ferguson A. M. N., Irwin M. J., Ibata R. A., Johnston K. V., Lewis G. F., Tanvir N. R., 2007, AJ, 133, 1275
Ferguson A. M. N., Irwin M. J., Ibata R. A., Lewis G. F., Tanvir N. R., 2002, AJ, 124, 1452
Ferguson A. M. N., Johnson R. A., 2001, ApJL, 559, L13
Ferguson A. M. N., Johnson R. A., Faria D. C., Irwin M. J., Ibata R. A., Johnston K. V., Lewis G. F., Tanvir N. R., 2005, ApJL, 622, L109
Font A. S., Johnston K. V., Guhathakurta P., Majewski S. R., Rich R. M., 2006, AJ, 131, 1436
Gallart C., Zoccali M., Aparicio A., 2005, ARA&A, 43, 387
Gallart C., Freedman W. L., Aparicio A., Bertelli G., Chiosi C., 1999, AJ, 118, 2245
Gauthier J.-R., Dubinski J., Widrow L. M., 2006, ApJ, 653, 1180
Gilbert K. M., et al., 2009, ApJ, 705, 1275
Girardi L., Bressan A., Bertelli G., Chiosi C., 2000, A&AS, 141, 371
Grevesse N., Noels A., 1993, in Prantzos N., Vangioni-Flam E., Cassé M., eds, Origin and Evolution of the Elements. Cambridge Univ. Press, Cambridge, p. 15
Harris J., Zaritsky D., 2001, ApJS, 136, 25
Hidalgo S. L., et al., 2011, ApJ, 730, 14
Holland S., Fahlman G. G., Richer H. B., 1996, AJ, 112, 1035
Ibata R., Chapman S., Ferguson A. M. N., Irwin M., Lewis G., McConnachie A., 2004, MNRAS, 351, 117
Ibata R., Chapman S., Ferguson A. M. N., Lewis G., Irwin M., Tanvir N., 2005, ApJ, 634, 287
Ibata R., Irwin M., Lewis G., Ferguson A. M. N., Tanvir N., 2001, Nature, 412, 49
Ibata R., Martin N. F., Irwin M., Chapman S., Ferguson A. M. N., Lewis G. F., McConnachie A. W., 2007, ApJ, 671, 1591
Ibata R. A., et al., 2014, ApJ, 780, 128
Innanen K. A., Kamper K. W., van den Bergh S., Papp K. A., 1982, ApJ, 254, 515
Irwin M. J., Ferguson A. M. N., Ibata R. A., Lewis G. F., Tanvir N. R., 2005, ApJL, 628, L105

Jarosik N., et al., 2011, ApJS, 192, 14
Kalirai J. S., et al., 2006, ApJ, 648, 389
Kazantzidis S., Bullock J. S., Zentner A. R., Kravtsov A. V., Moustakas L. A., 2008, ApJ, 688, 254
Kazantzidis S., Zentner A. R., Kravtsov A. V., Bullock J. S., Debattista V. P., 2009, ApJ, 700, 1896
Kniazev A. Y., Grebel E. K., Zucker D. B., Rix H., Martinez-Delgado D., Snedden S. A., 2013, AJ, 147, 16
Kroupa P., Tout C. A., Gilmore G., 1991, MNRAS, 251, 293
Kroupa P., 2002, Sci, 295, 82
Lewis G. F., et al., 2013, ApJ, 763, 4
Mayer L., Mastropietro C., Wadsley J., Stadel J., Moore B., 2006, MNRAS, 369, 1021
McConnachie A. W., 2005, PhD thesis, Institute of Astronomy, Cambridge University
McConnachie A. W., Irwin M. J., Ferguson A. M. N., Ibata R. A., Lewis G. F., Tanvir N., 2005, MNRAS, 356, 979
McConnachie A. W., Irwin M. J., Ibata R. A., Ferguson A. M. N., Lewis G. F., Tanvir N., 2003, MNRAS, 343, 1335
McConnachie A. W., Irwin M. J., Lewis G. F., Ibata R. A., Chapman S. C., Ferguson A. M. N., Tanvir N. R., 2004, MNRAS, 351, L94
McConnachie A. W. et al., 2009, Nature, 461, 66
Mighell K. J., 1999, ApJ, 518, 380
Monelli M., et al., 2010, ApJ, 720, 1225
Mori M., Rich R. M., 2008, ApJ, 674, L77
Mould J., Kristian J., 1986, ApJ, 305, 591
Nieten C., Neininger N., Guélin M., Ungerechts H., Lucas R., Berkhuijsen E. M., Beck R., Wielebinski R., 2006, A&A, 453, 459
Pietrinferni A., Cassisi S., Salaris M., Castelli F., 2004, ApJ, 612, 168
Purcell C. W., Bullock J. S., Kazantzidis S., 2010, MNRAS, 404, 1711
Quinn P. J., Hernquist L., Fullagar D. P., 1993, ApJ, 403, 74
Reitzel D. B., Guhathakurta P., Rich R. M., 2004, AJ, 127, 2133
Rich R. M., Reitzel D. B., Guhathakurta P., Gebhardt K., Ho L. C., 2004, AJ, 127, 2139
Richardson J. C. et al., 2008, AJ, 135, 1998
Sadoun R., Mohayaee R., Colin J., 2014, MNRAS, 442, 160
Schlegel D. J., Finkbeiner D. P., Davis M., 1998, ApJ, 500, 525
Sheffield A. A., et al., 2012, ApJ, 761, 161
Siegel M. H., et al., 2007, ApJ, 667, L57
Stetson P. B., 1994, PASP, 106, 250
Tanaka M., Chiba M., Komiyama Y., Guhathakurta P., Kalirai J. S., Iye M., 2010, ApJ, 708, 1168
Tanvir N. R., et al., 2012, MNRAS, 422, 162
Tissera P. B., Scannapieco C., Beers T. C., Carollo D., 2013, MNRAS, 432, 3391
Tolstoy E., Hill V., Tosi M., 2009, ARA&A, 47, 371
VandenBerg D. A., Bergbusch P. A., Dowler P. D., 2006, ApJS, 162, 375
Velazquez H., White S. D. M., 1999, MNRAS, 304, 254
Walker I. R., Mihos J. C., Hernquist L., 1996, ApJ, 460, 121
Walterbos R. A. M., Kennicutt R. C., Jr., 1988, A&A, 198, 61
Weisz D. R., Dolphin A. E., Skillman E. D., Holtzman J., Gilbert K. M., Dalcanton J. J., Williams B. F., 2014, ApJ, 789, 147
Williams B. F., 2002, MNRAS, 331, 293
Williams B. F., Dalcanton J. J., Dolphin A. E., Holtzman J., Sarajedini A., 2009, ApJ, 695, L15
Zucker D. B., et al., 2004, ApJ, 612, L117

APPENDIX A: SFHS OF INDIVIDUAL FIELDS

The results of the best-fitting SFHs for the remaining twelve fields are available as Supporting Information with the online version of the paper: disc-like fields in Figures A1–A4; stream-like fields in Figures A5–A8; and composite fields in Figures A9–A12.

This paper has been typeset from a TEX/ LATEX file prepared by the author.

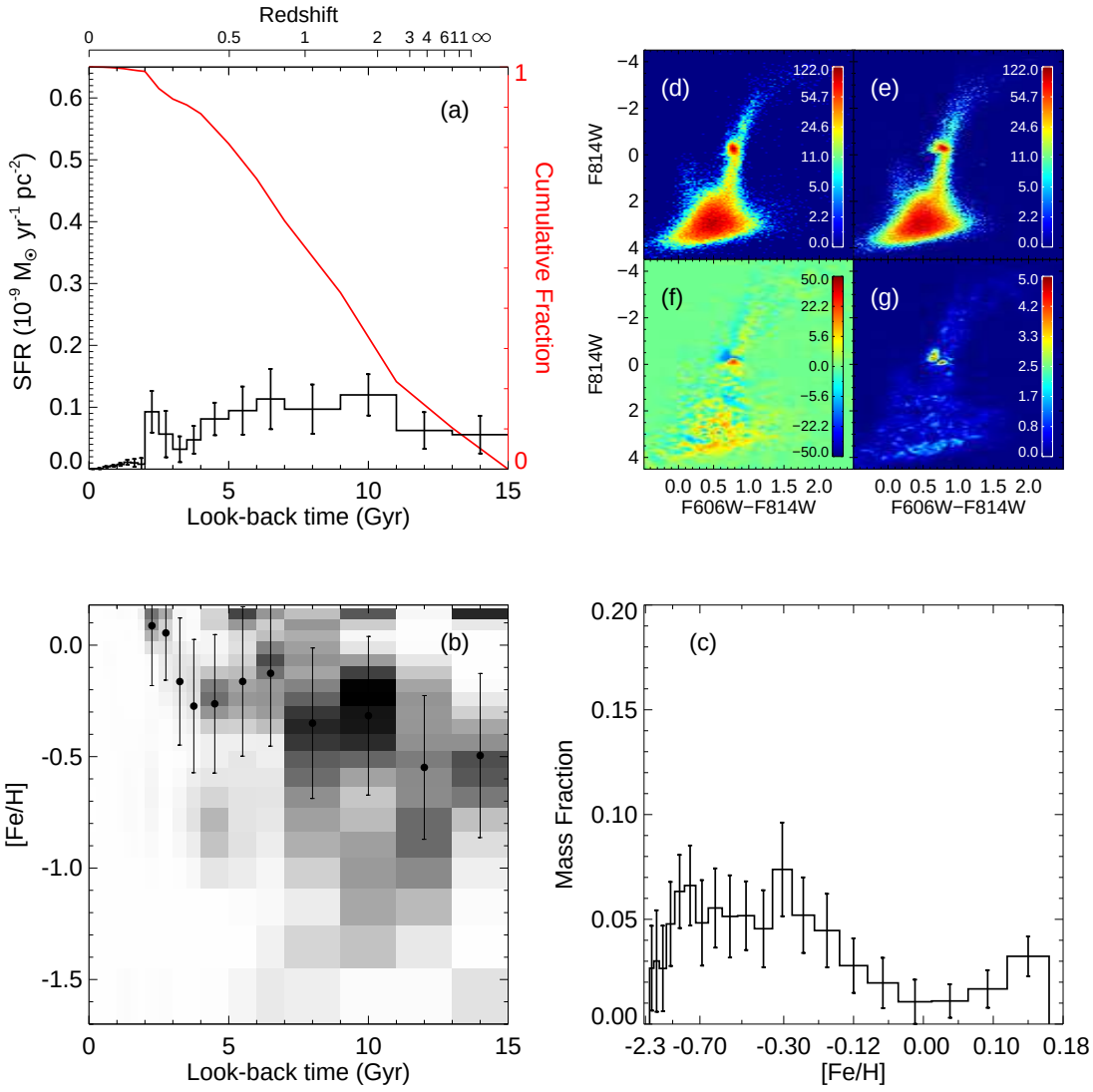

Figure A1. Best-fit SFH solution for the *Claw*. The panels show: (a) the SFR as a function of time, normalised to the deprojected area of the ACS field, (b) the AMR, where the grayscale is proportional to the *stellar mass* formed in each bin, (c) the metallicity distribution of the mass of stars formed, (d)-(e) the Hess diagrams of the observed and best-fit model CMDs, (f) the residuals, and (g) the significance of the residuals in Poisson σ. The cumulative mass fraction is shown in red in panel (a). The filled circles and error bars in panel (b) show the median metallicity and standard deviation in age bins representing at least 1 percent of the total mass of stars formed.

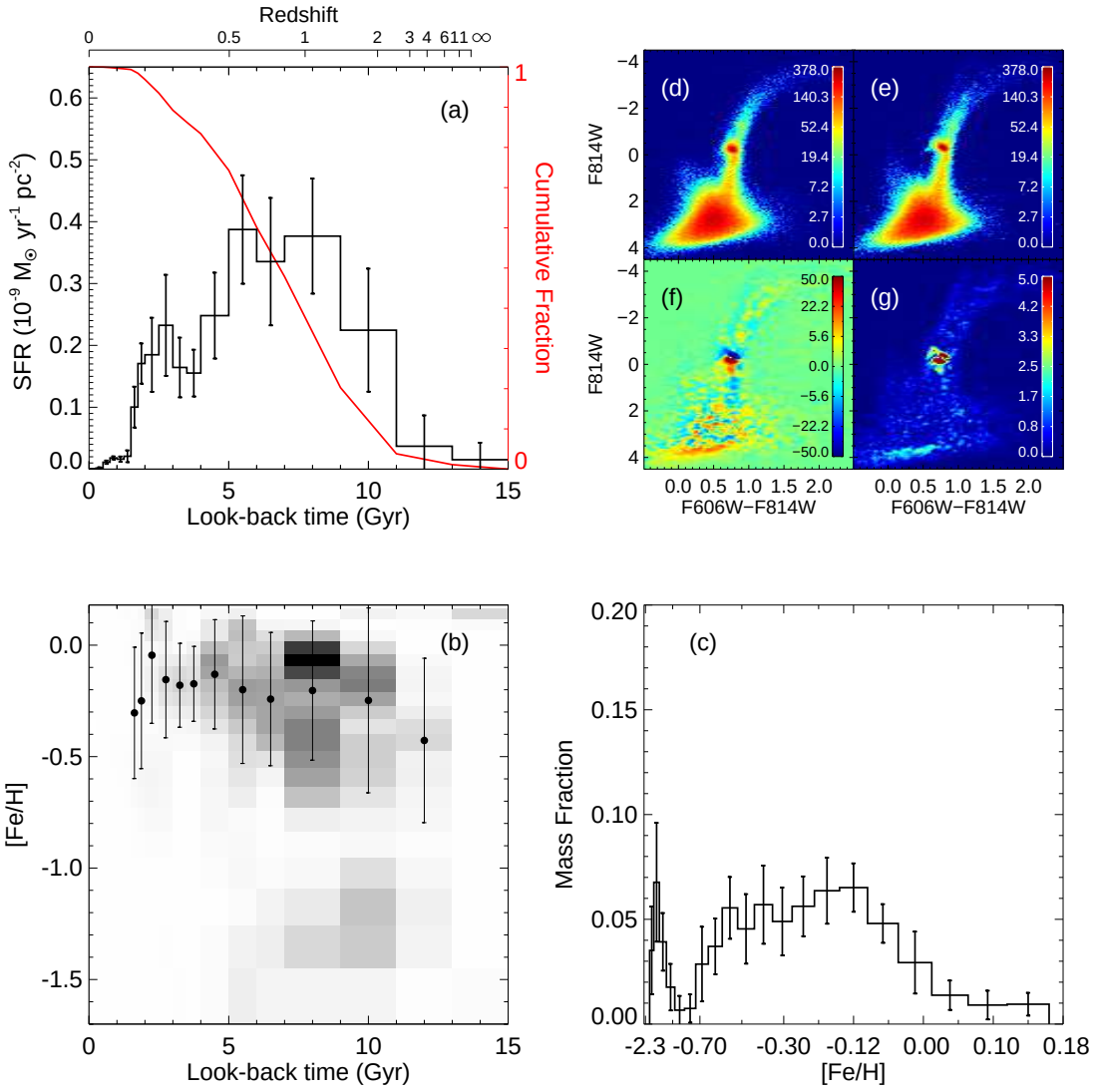

Figure A2. Same as Fig. AA1, but for the *NSpur*.

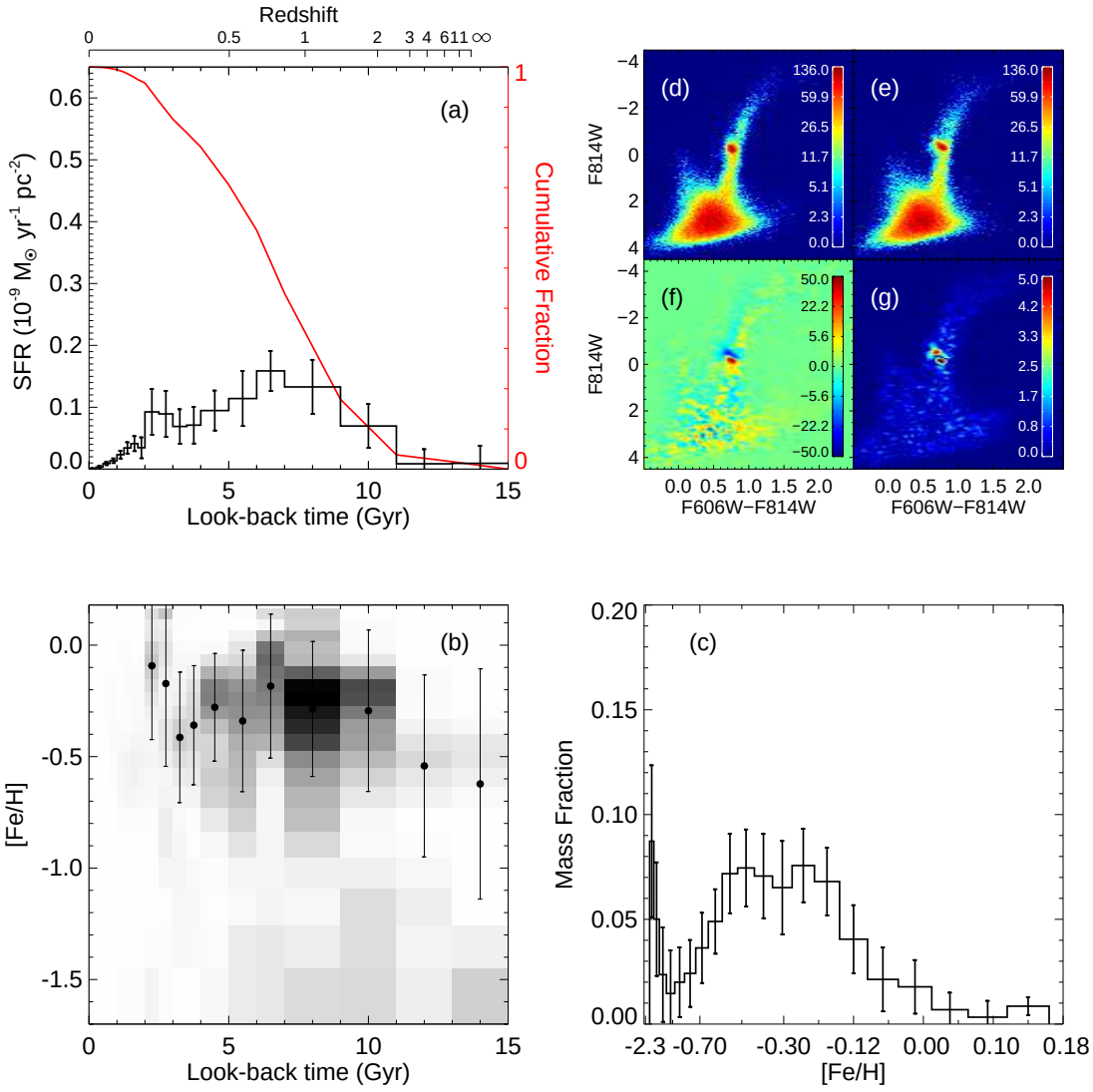

Figure A3. Same as Fig. AA1, but for the *G1 Clump*.

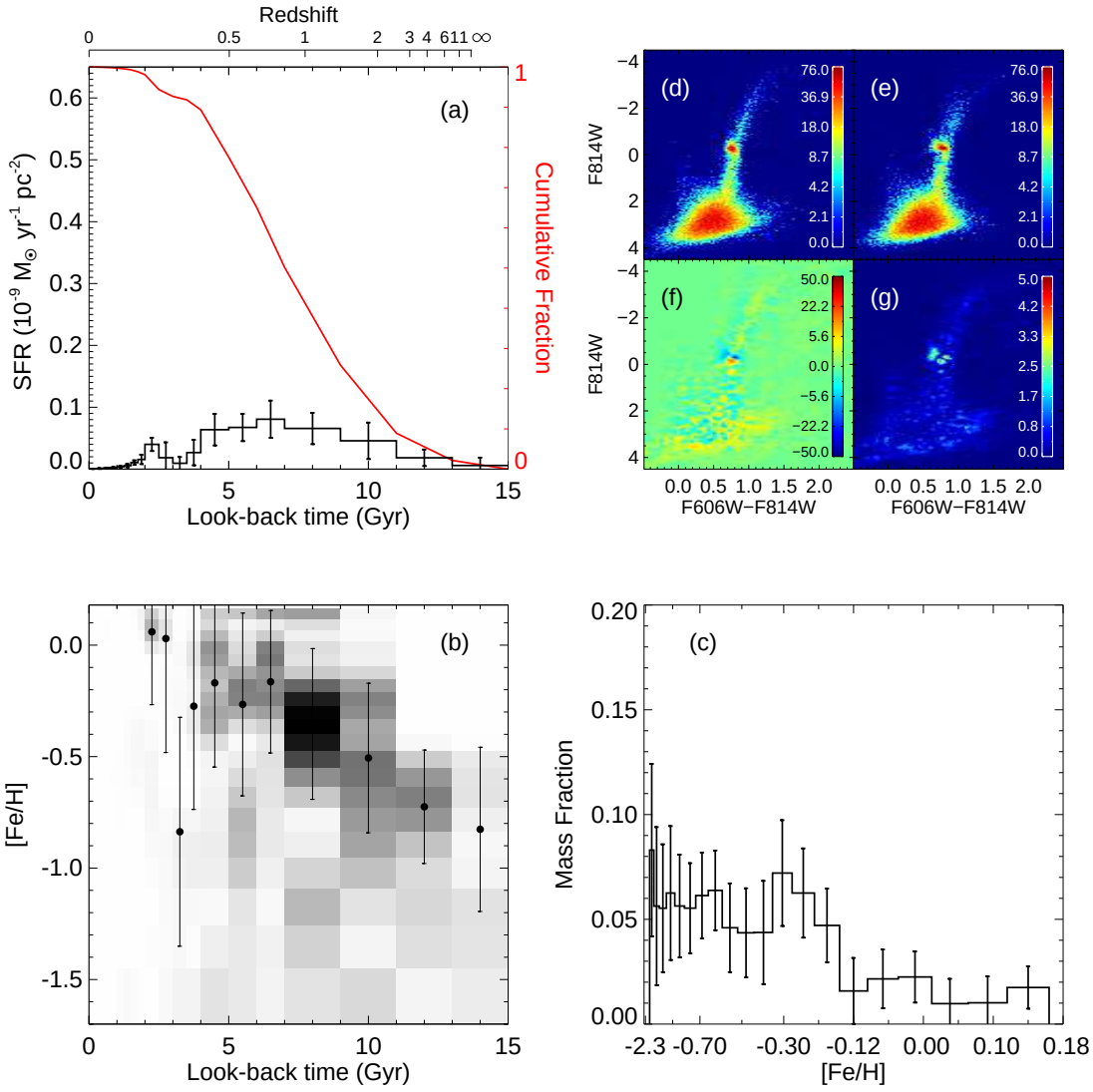

Figure A4. Same as Fig. AA1, but for the *NE Clump*.

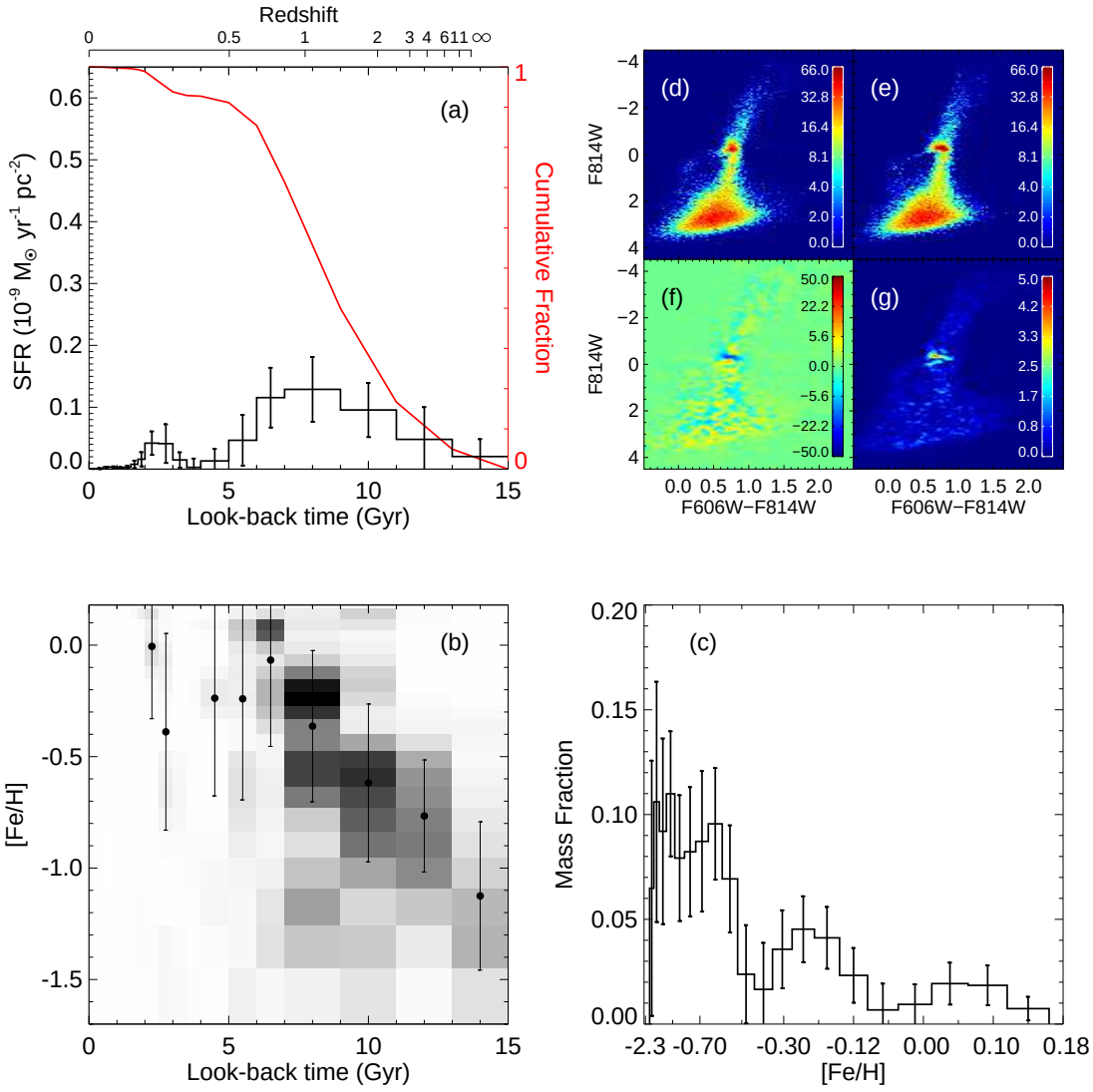

Figure A5. Same as Fig. AA1, but for the *EC1_field*.

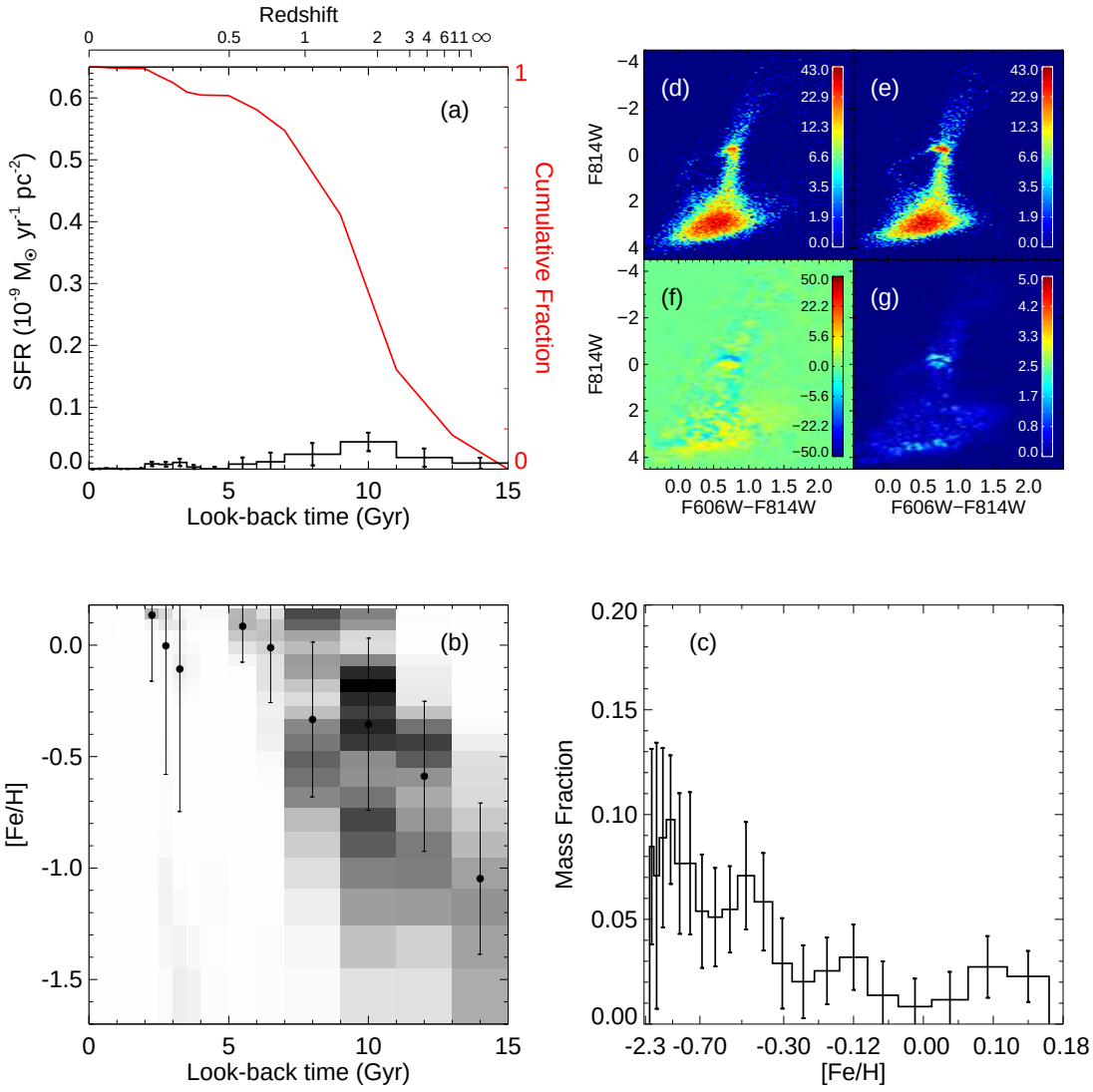

Figure A6. Same as Fig. AA1, but for the *Minor axis*.

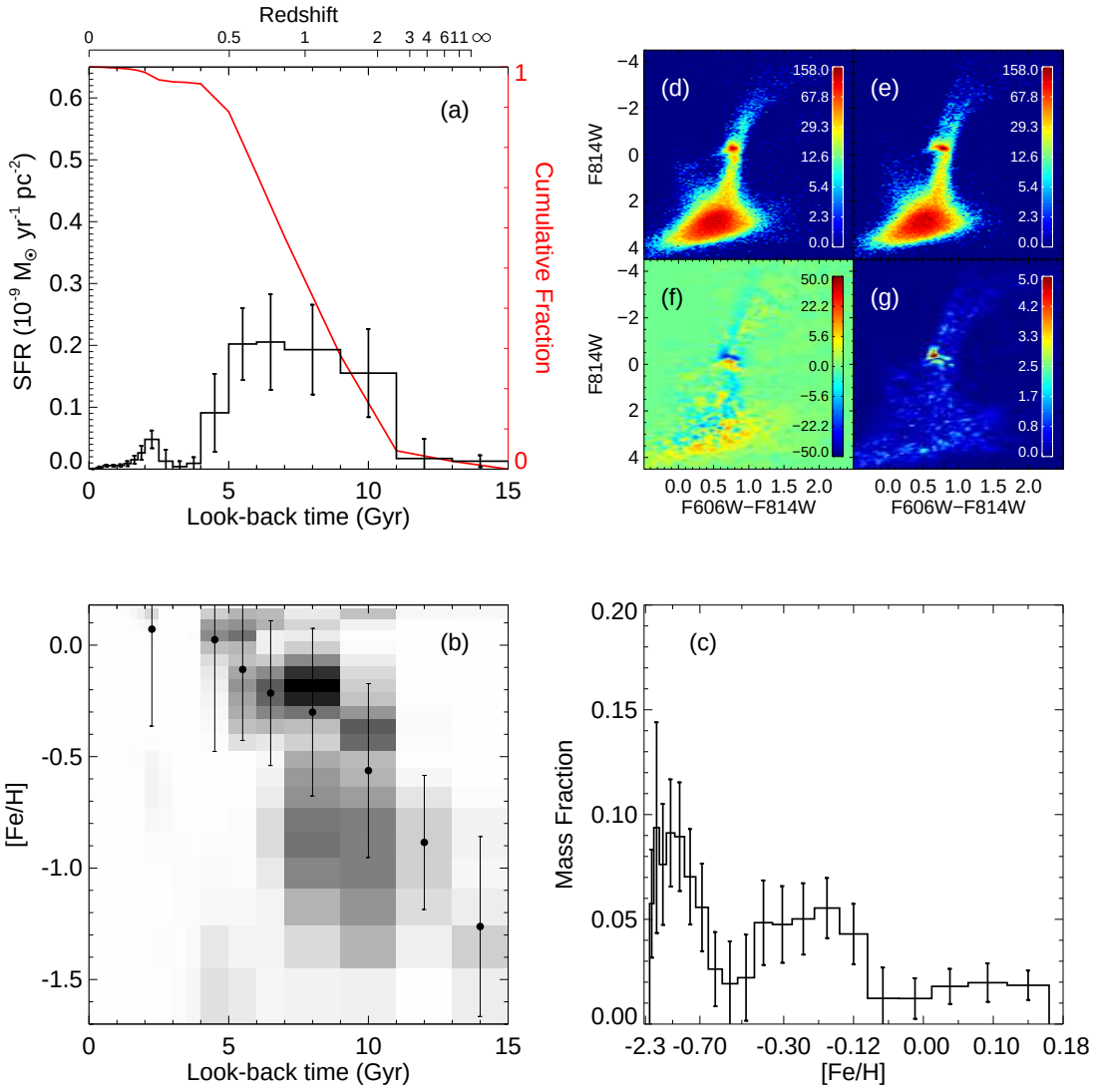

Figure A7. Same as Fig. AA1, but for the *NE Shelf*.

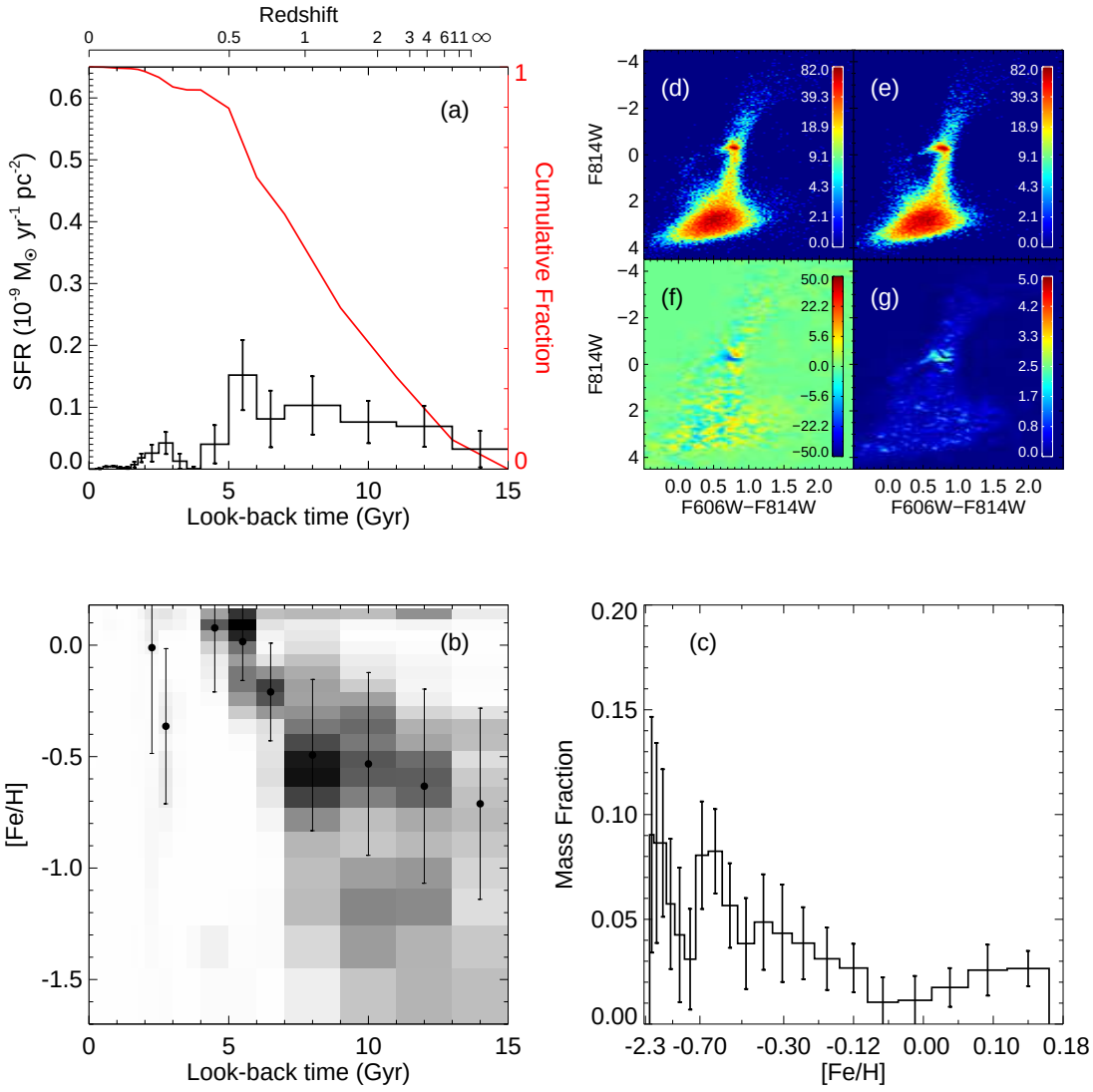

Figure A8. Same as Fig. AA1, but for the *Brown-stream*.

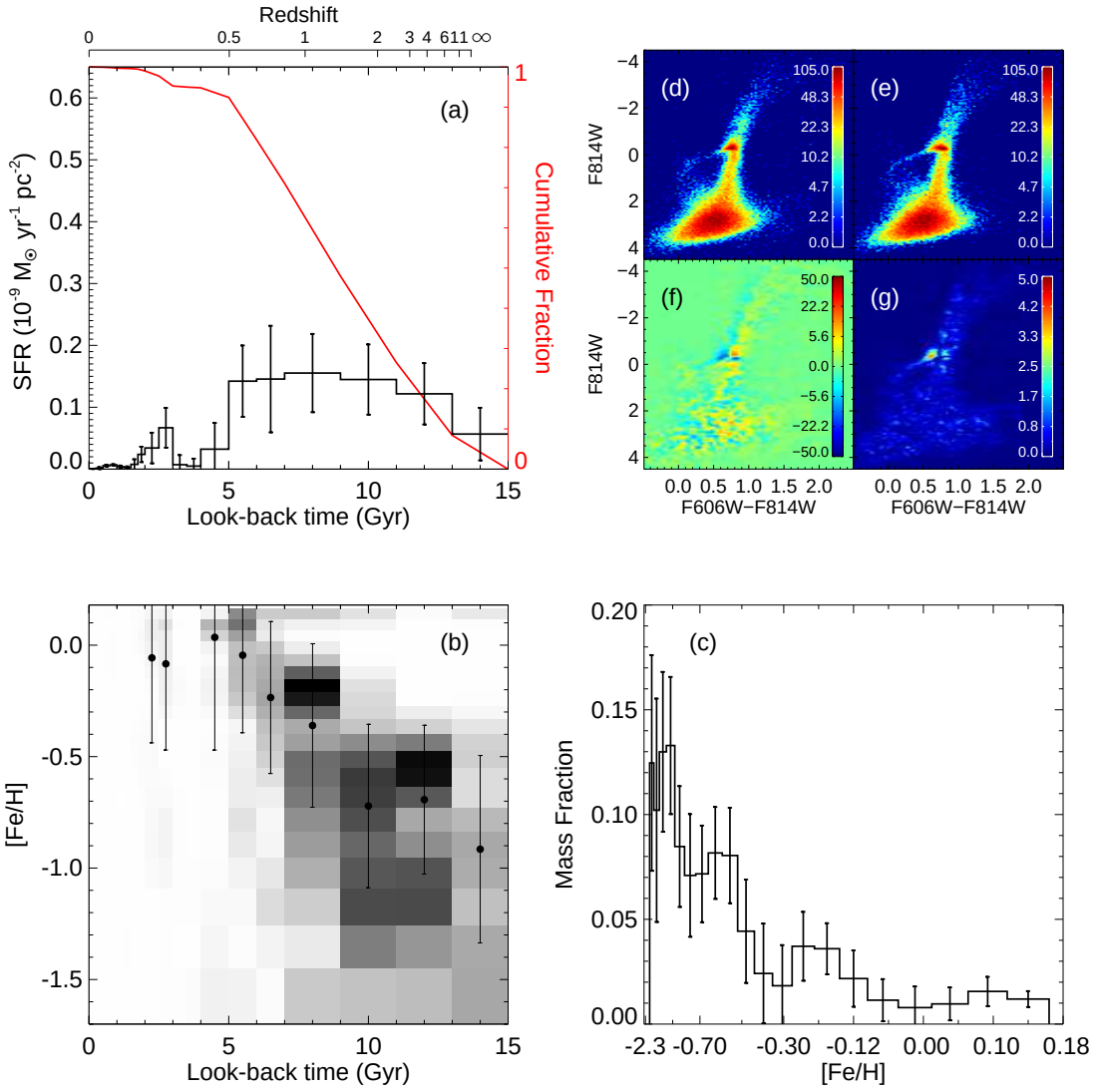

Figure A9. Same as Fig. AA1, but for the *Brown-spheroid*.

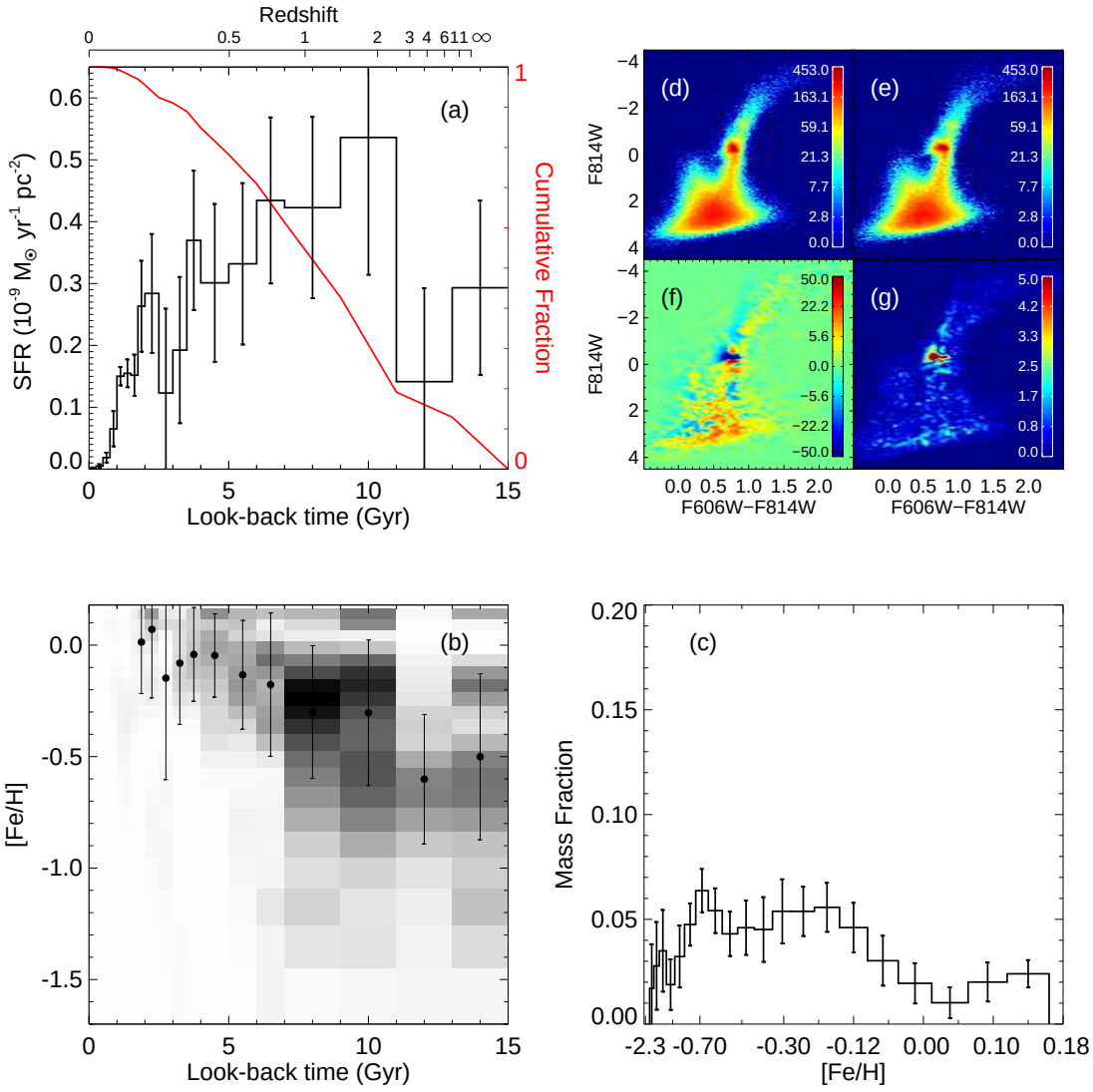

Figure A10. Same as Fig. AA1, but for the *GC6_field*.

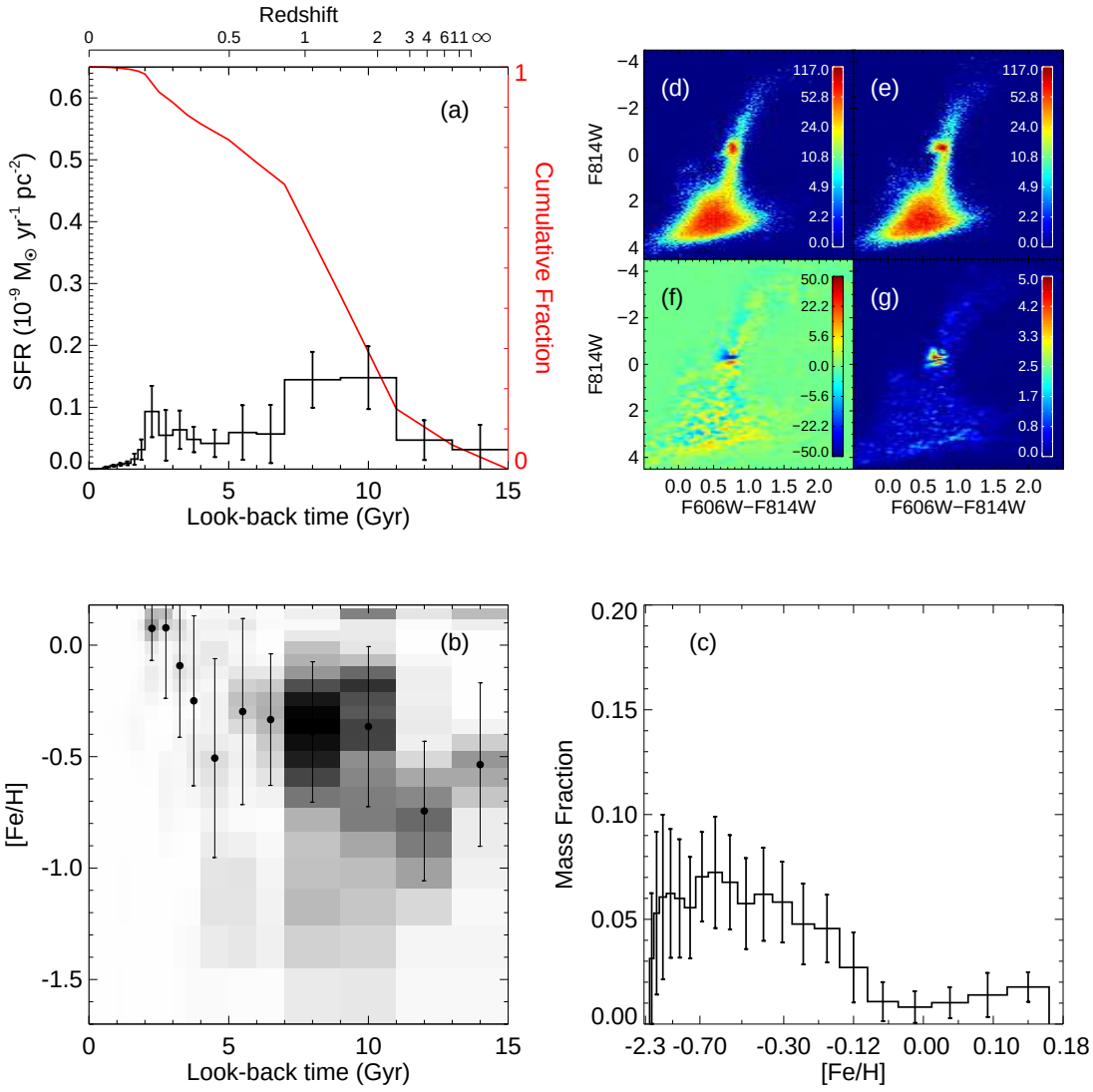

Figure A11. Same as Fig. AA1, but for the *NGC 205 Loop*.

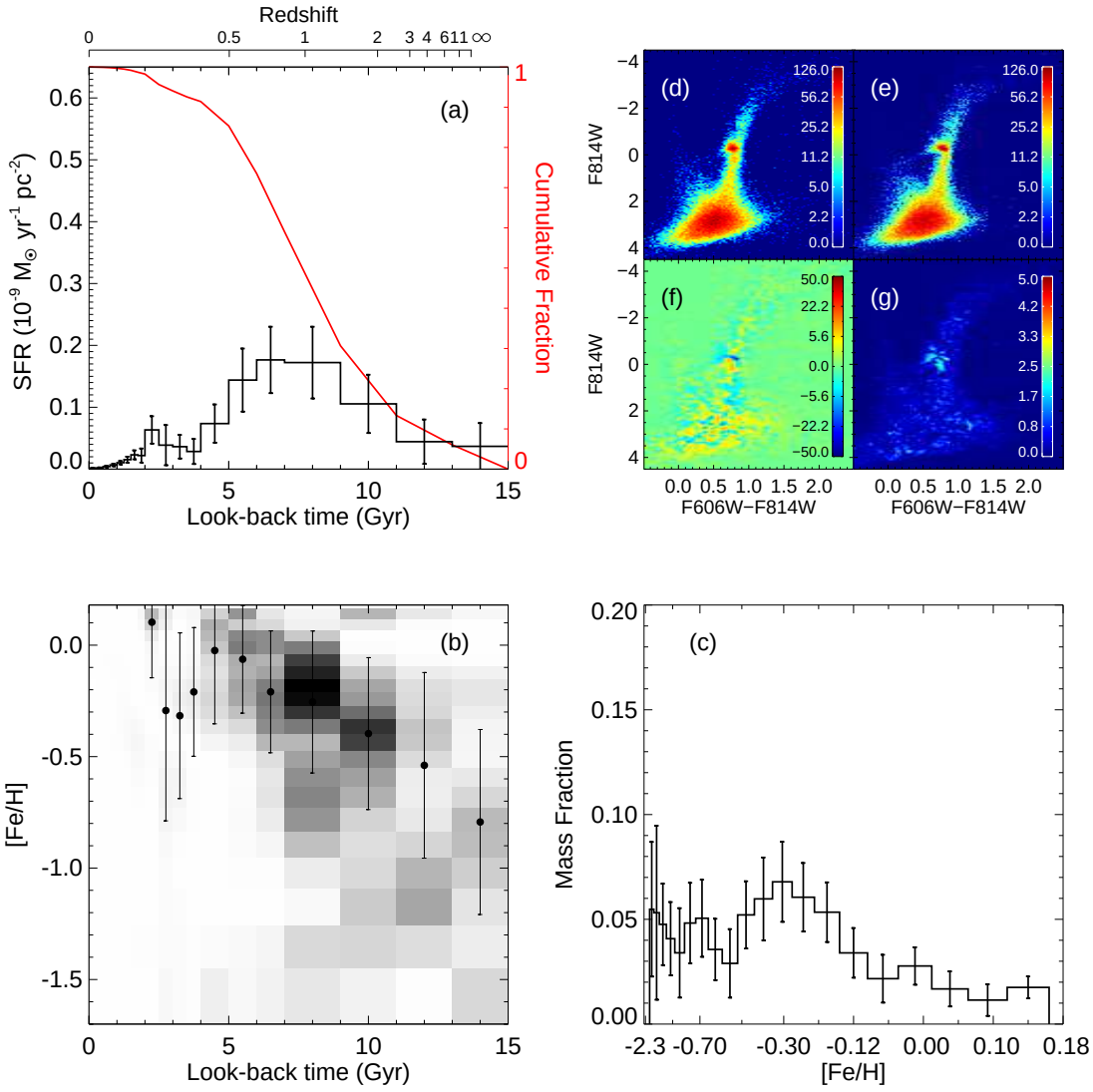

Figure A12. Same as Fig. AA1, but for the *Brown-disk*.